The COBE Diffuse Infrared Background Experiment Search for the Cosmic Infrared Background: III. Separation of Galactic Emission from the Infrared Sky Brightness

R. G. Arendt,^{1,2} N. Odegard,² J. L. Weiland,² T. J. Sodroski,³ M. G. Hauser,⁴ E. Dwek,⁵ T. Kelsall,⁵ S. H. Moseley,⁵ R. F. Silverberg,⁵ D. Leisawitz,⁶ K. Mitchell,⁷ W. T. Reach,⁸ E. L. Wright⁹

submitted to The Astrophysical Journal received: 8 January 1998, accepted: 12 May 1998

ABSTRACT

The Cosmic Infrared Background (CIB) is hidden behind veils of foreground emission from our own solar system and Galaxy. This paper describes procedures for removing the Galactic IR emission from the 1.25 – $240~\mu m$ COBE DIRBE maps as steps toward the ultimate goal of detecting the CIB. The Galactic emission models are carefully chosen and constructed so that the isotropic CIB is completely retained in the residual sky maps. We start with DIRBE data from which the scattered light and thermal emission of the interplanetary dust (IPD) cloud have already been removed. Locations affected by the emission from bright compact and stellar sources are excluded from the analysis. The unresolved emission of faint stars at near- and mid-IR wavelengths is represented by a model based on Galactic source counts. The $100~\mu m$ DIRBE observations are used as the spatial template for the interstellar medium (ISM) emission at

¹email: arendt@stars.gsfc.nasa.gov

²Raytheon STX, Code 685, NASA GSFC, Greenbelt, MD 20771

³Space Applications Corp., Code 685, NASA GSFC, Greenbelt, MD 20771

⁴Space Telescope Science Institute, 3700 San Martin Drive, Baltimore MD, 21218

⁵Code 685, NASA GSFC, Greenbelt, MD 20771

⁶Code 631, NASA GSFC, Greenbelt, MD 20771

⁷General Sciences Corp., Code 920.2, NASA GSFC, Greenbelt, MD 20771

⁸IPAC, Caltech, MS 100-22, Pasadena, CA 91125

⁹UCLA, Department of Astronomy, Los Angeles, CA 90024-1562

high latitudes. Correlation of the 100 μ m data with H I column density allows us to isolate the component of the observed emission that is associated with the ISM. Limits are established on the far-IR emissivity of the diffuse ionized medium, which indicate a lower emissivity per H nucleus than in the neutral medium. At 240 μ m, we find that adding a second spatial template to the ISM model can greatly improve the accuracy of the model at low latitudes. The crucial product of this analysis is a set of all-sky IR maps from which the Galactic (and IPD) emission has been removed. We discuss systematic uncertainties and potential errors in the foreground subtraction process that may have an impact on studies seeking to detect the CIB in the residual maps.

Subject headings: diffuse radiation — Galaxy: general — infrared: ISM: continuum — infrared: stars — ISM: general

1. Introduction

The primary scientific goal of the Diffuse Infrared Background Experiment (DIRBE) aboard the Cosmic Background Explorer (COBE) spacecraft is the measurement of the cosmic infrared background (CIB) at wavelengths from 1.25 to 240 μ m. This radiation is the cumulative emission of pregalactic sources, protogalaxies, and evolving galaxies, as well as emission from more exotic processes not common in the local universe (e.g. Bond, Carr, & Hogan 1986). These sources of the CIB may be found anywhere from the earliest epoch after radiation and matter were decoupled to the present day. The contribution to the CIB from galaxies will be composed of stellar emission from distant galaxies that is redshifted by the cosmological expansion from intrinsically shorter wavelengths, as well as the direct IR emission from stars and dust within galaxies at all distances. The constraints that DIRBE places on the CIB are discussed by Hauser et al. (1998, hereafter Paper I) and Dwek et al. (1998, hereafter Paper IV).

However, in order to detect the CIB, we first need to remove the strong contributions of foreground emission arising within our own solar system and Galaxy. The IR foreground from within our solar system originates from the interplanetary dust (IPD) cloud. The modeling and removal of the scattering and emission from the IPD for the entire cold-mission DIRBE data set are reported by Kelsall et al. (1998, hereafter Paper II). Following the removal of this foreground, we attack the next layer of foreground emission by modeling and subtracting the Galactic IR emission.

The near-IR $(1.25-4.9~\mu\text{m})$ emission of the Galaxy is dominated by starlight. Some bright stars and other compact sources are resolved as point sources in the DIRBE data. Most stars blend into a diffuse background, showing a disk and bulge very similar in appearance to many edge-on spiral galaxies. Extinction effects are clearly present at the shortest near-IR wavelengths as a visible dark lane in the inner Galaxy. Papers which have previously examined DIRBE observations of the stellar disk and bulge of the Galaxy are: Weiland et al. (1994), Arendt et al. (1994), Freudenreich et al. (1994), Dwek et al. (1995), Calbet et al. (1996), Freudenreich (1996), Binney, Gerhard, & Spergel (1997), Bissantz et al. (1997), Porcel, C., Battaner, E., & Jiménez-Vicente, J. (1997), and Fux (1997). The mid- and far-IR (12 – 100 and 140 – 240 μ m) emission is dominated by thermal emission from dust in the diffuse ISM and in more compact star-forming regions. Previously published studies of the Galactic ISM based on DIRBE data include: Arendt et al. (1994), Freudenreich et al. (1994), Sodroski et al. (1994, 1995), Bernard et al. (1994), Boulanger et al. (1996), Dwek et al. (1997), Sodroski et al. (1997), Davies et al. (1997), and Lagache et al. (1998).

This paper details the development of models of the Galactic IR emission. The primary intended use for the models is to permit an accurate measurement of an extragalactic IR background. The characterization of the sources that give rise to the Galactic emission is an important secondary result of the process. An overview of the procedures used for modeling the Galactic foreground is given in Section 2. Section 3 describes the DIRBE data set and its preparation, particularly the removal of the IPD scattering and emission (Paper II). Section 4 describes the modeling and removal of starlight from the 1.25 to 25 μ m measurements. The following section (§5) describes in detail the modeling and removal of the ISM emission from DIRBE data. Additional investigation into the far-IR emissivity of the diffuse ionized ISM is contained in the Appendix. The accuracy of the removal of the Galactic emission is a major limitation to the detection of the CIB, and consequently Section 6 discusses estimates of the uncertainties of the data and procedures. A brief discussion of the implications of this modeling for Galactic properties is contained in Section 7. A more detailed analysis of the Galactic ISM as revealed by this work has been reported by Dwek et al. (1997). Finally, a brief summary of results is given in Section 8. Companion papers (Papers I & IV) contain analyses of the residual emission, and its implications for the detection of the CIB.

2. Methods

We will assume that at any time, t, the total intensity observed at a given wavelength and a specified Galactic longitude and latitude, $I_{obs}(l, b, \lambda, t)$, can be represented by:

$$I_{obs}(l, b, \lambda, t) = Z(l, b, \lambda, t) + G_S(l, b, \lambda) + G_I(l, b, \lambda) + I_0(l, b, \lambda)$$
(1)

where $Z(l, b, \lambda, t)$ is the contribution from the interplanetary dust cloud, $G_S(l, b, \lambda)$ is the contribution from stars (resolved and unresolved) and other compact sources within the Galaxy, $G_I(l, b, \lambda)$ is the contribution from the interstellar medium, and $I_0(l, b, \lambda)$ is residual intensity obtained by subtracting the former three components from the total observed intensity. The procedures we apply are designed to ensure that the CIB is fully contained within this residual emission, i.e., that no CIB component is inadvertently included in the models of the IPD cloud or Galactic emission components.

The contribution of the IPD to the infrared sky, $Z(l, b, \lambda, t)$, has been calculated in Paper II. The IPD cloud is modeled using a geometric kernel similar to that developed to represent IPD emission in the IRAS data (Wheelock et al. 1994). The model ensures the preservation of the CIB intensity by fitting the time variation of the IPD emission rather than the intensity directly. The model does not contain any explicit isotropic component which would produce no time variation. Details of this model are presented in Paper II.

In the DIRBE data, the stellar emission component of the Galaxy, $G_S(l, b, \lambda)$, consists of two components: the first is a discrete component, which includes all bright sources that exceed the local background level by a chosen amount, depending on wavelength; and the second is a smooth component, consisting of unresolved stellar sources which can be represented by using a statistical model for calculating the brightness of the Galaxy.

Rather than modeling and removing each of the bright sources at all wavelengths, the locations of these sources are simply blanked and excluded from any further processing or analysis. Sources excluded by this procedure consist of bright stars at short wavelengths, and diffuse sources such as the Magellanic Clouds and bright star-forming regions in the Galactic plane (e.g. the ρ Oph and Orion regions), which appear at all wavelengths. The procedure for constructing the bright source removed maps is described in detail in Section 4.1.

The unresolved stellar emission component is represented by a "Faint Source Model," which closely follows the "SKY" model described by Wainscoat et al. (1992), and further developed by Cohen (1993a, 1994a, 1995). The SKY model of Galactic structure was originally developed to fit ground-based K-band and V-band and IRAS 12 and 25 μ m Galactic source counts. The fitting of source counts of known types of objects, instead

of total intensity measurements, ensures that the model intensity represents that of the Galactic sources, thereby excluding any possible unresolved extragalactic contribution.

To guarantee that the modeled ISM contribution to the sky brightness includes only Galactic emission, we will write this emission component, $G_I(l,b,\lambda)$, as a product of a spatially invariant spectral component $R(\lambda)$ times a wavelength-independent spatial template. The spatial template, such as the Galactic H I or CO column density, is associated with the Galactic gas phase component in which the dust resides. The advantage of such a procedure is that the line emission from most extragalactic sources is redshifted to velocities higher than those at which Galactic line emission is observed. Thus, the H I and CO data can be used as templates of the local (Galactic) IR emission of the ISM, without any contributions from extragalactic sources. In principle, $R(\lambda)$ can be obtained directly as the slope of a linear least squares fit to the correlation of $I_{ZG_S}(l,b,\lambda) \equiv I_{obs}(l,b,\lambda) - Z(l,b,\lambda) - G_S(l,b,\lambda)$ with the H I or CO spatial template for all wavelengths λ . The intercept will then yield the value of $I_0(l,b,\lambda)$. However, the main limitations to such a direct approach are: that there can be relatively large spatial variations in $R(\lambda)$, the IR emission per H atom; and that high-quality H I and CO data sets have restricted sky coverage or different spatial resolution compared to the DIRBE data. These limitations can be circumvented by using the 100 μ m ISM emission $G_I(l, b, 100)$ μ m) as the spatial template for ISM emission at the other wavelengths. The subtraction of the interstellar component was therefore performed in the following manner. First, $R(\lambda)$ and $I_0(l, b, 100 \ \mu \text{m})$ were obtained as the slope and intercept of the correlation between $I_{ZG_S}(l, b, 100 \ \mu \text{m})$ and the H I spatial template. This step allows us to separate the ISM emission, $G_I(l, b, 100 \ \mu\text{m}) \equiv I_{obs}(l, b, 100 \ \mu\text{m}) - Z(l, b, 100 \ \mu\text{m}) - I_0(l, b, 100 \ \mu\text{m})$, from the potential CIB, $I_0(l, b, 100 \ \mu \text{m})$. Then, we chose $G_I(l, b, 100 \ \mu \text{m})$ as the spatial template, and calculated $R(\lambda)$ by correlating this template with $I_{ZG_S}(l, b, \lambda \neq 100 \ \mu\text{m})$, so that $G_I(l, b, \lambda) = R(\lambda) \times G_I(l, b, 100 \ \mu \text{m}).$

For the near-IR wavelengths ($\lambda \leq 4.9 \ \mu m$), the subtraction of the starlight is not sufficiently accurate to yield values of $R(\lambda)$ and $I_0(l,b,\lambda)$ from direct correlations of the near-IR data with $G_I(l,b,100 \ \mu m)$. However, the dust emission in the near-IR can be more easily distinguished from the stellar emission in color-color plots (e.g., Arendt et al. 1994), as points that are displaced from the reddening line for stellar emission. This aspect of the subtraction of the ISM-related near-IR emission is described in detail in Section 5.5.

3. DIRBE Data and the Infrared Emission from the Interplanetary Dust Cloud

The DIRBE instrument provides absolutely calibrated intensity sky maps in 10 broad bands at 1.25, 2.2, 3.5, and 4.9 μ m (near-IR), 12, 25, 60, and 100 μ m (mid-IR), and 140 and 240 μ m (far-IR). The instrumental zero point is established by chopping between the sky and a cold zero-flux reference source at 32 Hz. Frequent observations of internal reference sources and stable celestial sources allow corrections for small instrumental gain instabilities on both short and long time scales. Measurements of a few well-calibrated celestial sources (Sirius for 1.25 – 12 μ m, NGC 7027 for 25 μ m, Uranus for 60 and 100 μ m, and Jupiter for 140 and 240 μ m) provide the absolute calibration of the DIRBE photometric system. Further details on the calibration of the data can be found in the *COBE* DIRBE Explanatory Supplement (1997).

The DIRBE time-ordered data are pixelized and mapped in the COBE sky-cube format (COBE DIRBE Explanatory Supplement 1997). All analysis is performed on maps in this coordinate system. For illustrational purposes, maps shown in this paper are reprojected into a Galactic Mollweide projection. The Mollweide projection is an equal-area projection with the convenient properties that longitudes are equally spaced (for a fixed latitude) and all lines of constant latitude are straight horizontal lines (though unequally spaced). The DIRBE surface brightness maps are presented in units of MJy/sr, which can be converted to νI_{ν} intensities in units of nW m⁻² sr⁻¹ through multiplication by $3000/\lambda$, where λ is the wavelength of the band in μ m.

The sky was scanned by DIRBE in a manner that provided highly redundant coverage over a 60° wide swath in a single week. The viewing swath samples solar elongation angles from roughly 64° to 124° , and precesses with an annual period. The DIRBE beam is $\sim 0.7 \times 0.7$ at all wavelengths. A more complete description of the DIRBE instrument has been given by Silverberg et al. (1993) and the COBE DIRBE Explanatory Supplement (1997). The COBE mission is described by Boggess et al. (1992).

The highly redundant coverage per line of sight and wide range of solar elongation angles sampled provide an excellent database for purposes of modeling the IPD foreground in order to remove it from DIRBE observations. We use the parametric geometrical model described by Paper II to compute the signal from the interplanetary dust cloud, denoted here as Z, for each line-of-sight (pixel) in the DIRBE maps. Components of the model are a smooth dust cloud, three pairs of dust bands, and a circumsolar ring in earth-orbit resonance. Details on the construction of this model and on the accuracy of its results are presented in Paper II.

Maps of the intensity after subtraction of the IPD emission and scattered sunlight are shown in Galactic Mollweide projection in Figure 1. These data available as the 'Zodi-Subtracted Mission Average (ZSMA)' maps, through the NSSDC *COBE* homepage website at http://www.gsfc.nasa.gov/astro/cobe/cobe_home.html.

4. Infrared Emission from the Stellar Galactic Component

4.1. Bright Source Removal

In order to model and remove the Galactic foreground emission on the largest angular scales, we excluded small localized regions that are much brighter (and often had distinctly different properties) than the average Galactic foreground. These regions mainly consist of bright stars at the near-IR wavelengths, star forming regions at mid- and far-IR wavelengths, and a few nearby external galaxies [See Odenwald, Newmark, & Smoot (1997) for an analysis of the external galaxies visible to DIRBE]. The locations of these bright sources have been individually blanked from the maps, and were excluded from further analysis. Even though the intensities in the unblanked pixels are left unchanged, the mean intensity over large areas is reduced by the bright source blanking because the brightest pixels are now excluded.

A number of bright source identification algorithms were tested, both for speed of execution and for source detection accuracy. We adopted an algorithm based upon pixel brightness relative to a locally determined smooth background. The smooth background level for each pixel in the map was computed using a morphological filter (the "opening" operation; see Haralick, Sternberg & Zhuang 1987), followed by a linear smoothing. Pixels in the original map where the brightness exceeded the background level by more than a fixed threshold were blanked. These thresholds are: 15, 15, 15, 15, 85, 110 Jy for point sources at 1.25, 2.2, 3.5, 4.9, 12, and 25 μm respectively and 4.5 MJy sr⁻¹ = 135 nW m⁻² sr⁻¹ for the more extended sources found at 100 μ m. The 60, 140, and 240 μ m maps were blanked at the same locations as the 100 μ m map. Because the DIRBE beam is larger than a standard pixel ($\sim 0.32 \times 0.32$), the four nearest neighbor pixels were blanked as well. Circular regions around the Large and Small Magellanic Clouds were blanked at all wavelengths. The fraction of the sky above $|b| = 30^{\circ}$ that is excluded by the bright source removal ranges from $\sim 35\%$ at the shortest wavelengths to <1% at $\lambda > 60 \ \mu m$. Figure 2 shows the map of 2.2 μ m intensity after the contribution of the IPD has been removed and the bright source blanking has been applied (cf. Fig. 1). All subsequent intensity maps will contain black regions indicating the locations where bright sources have been blanked.

This source removal technique does not work well at low Galactic latitudes, where both source confusion and the curvature of the background are high. In tests on simulated maps, however, the method was completely successful in blanking sources above $|b| = 20^{\circ}$. Further tests showed that varying the threshold level by $\pm 20\%$ (a generous estimate of the map noise) changed the median brightness of the sky above $|b| = 15^{\circ}$ by well under one percent at 1.25 and 2.2 μ m, and even less at the other wavelengths.

4.2. The Faint Source Model

After the bright sources are removed by blanking, most of the residual diffuse near-IR emission is starlight from unresolved sources. These sources are sufficiently numerous and evenly distributed that a statistical model well represents their collective emission. To remove the Galactic diffuse stellar emission component we constructed a "Faint Source Model" (FSM) of the integrated brightnesses in the DIRBE 1.25, 2.2, 3.5, 4.9, 12 and 25 μ m bands, based on the statistical model developed by Wainscoat et al. (1992). Subsequent improvements to the Wainscoat et al. "SKY" model by Cohen (1993a, 1994a, 1995) are generally not included in the FSM because they do not pertain to emission at near-IR wavelengths or because they are not specified in detail such that they can be accurately reproduced within the framework of the FSM. The FSM can be used to calculate the surface brightness in any direction of the sky by integrating the flux emitted by the various stellar components along that line of sight. If the Galaxy consisted of a single type of star, with a corresponding absolute magnitude M_{ν} , then the sky brightness along a line of sight would be given by:

$$I_{\nu} = \frac{L_{0\nu} 10^{-0.4M_{\nu}}}{4\pi} \int_{0}^{\infty} e^{-\tau(s)} n(x, y, z) ds$$
 (2)

where n(x, y, z) is the number density of sources at a given position in the Galaxy which is integrated along the line of sight s, $\tau(s)$ is the optical depth along the line of sight, and $L_{0\nu}$ is the luminosity of a zero magnitude star. A more realistic representation of the sky brightness must include a summation over many different stellar types and their spatial distributions. The simple expression (Eq. 2) is then replaced by the more complicated one:

$$I_{\nu} = \frac{1}{4\pi} \sum_{i} \sum_{j} \int_{0}^{\infty} e^{-\tau(s)} n(x, y, z, i, j) L_{0\nu}(i) \int_{\Delta M_{\nu}(i)} \omega(M_{\nu}, i) 10^{-0.4 M_{\nu}(i)} dM_{\nu} ds$$
 (3)

where the summations over i and j represent, respectively, those over stellar types, and over Galactic structural components, and the integral over M_{ν} represents the fact that stars of a given type have an intrinsic dispersion $\Delta M_{\nu}(i)$ in absolute magnitudes centered on $M_{\nu}(i)$ with a probability $\omega(M_{\nu}, i)$. The FSM follows the basic form of the Wainscoat et al. and SKY models, including 5 structural components for the Galaxy (disk, spiral arms, molecular ring, bulge, and halo), 87 source types, each with a dispersion of absolute magnitudes, and interstellar extinction from dust in an exponential (in radius and scale height, z) disk. The spiral arm component includes the local spur as defined by Cohen (1994a).

We have made several modifications to our FSM, deviating from the SKY model, either out of necessity or to produce results more suited for comparison with the DIRBE data:

- a) Since source count models cannot accurately represent the brightest point sources, which are unevenly distributed across the sky, the FSM was only integrated over stars fainter than those that were previously blanked from the DIRBE maps. The value of the brightness limit at which the bright source blanking stops and the Faint Source Model begins is not a significant source of uncertainty. Changes in the limits by 20% produce <5% changes in the Faint Source Model intensities, which are largely offset by complementary changes in the flux excluded by the bright source blanking (Section 4.1.).
- b) We have increased the spatial resolution of the model and calculated the sky brightness at the resolution of the DIRBE maps.
- c) The halo is described by Wainscoat et al. (1992) only as an $R^{1/4}$ law in projected surface brightness. Therefore we have adapted the formulation for the volume density presented by Young (1976) for use in our Faint Source Model. At high Galactic latitudes, the halo is the third most important component of the Faint Source Model after the disk and the spiral arms.
- d) We omitted the extragalactic component of the SKY model, which contributes mainly at faint magnitudes at 25 μ m (Cohen 1994a).
- e) The position of the Sun was set at 18 pc above the midplane of the Galactic disk. This was determined during preliminary trials, by requiring equal brightnesses at the north and south Galactic poles after subtraction of the FSM in the near IR bands. This value is independently supported by analysis done with the SKY model (Cohen 1995).
- f) For 3.5 and 4.9 μ m absolute magnitudes, which are not represented in the Wainscoat et al. (1992) source table, we obtained approximate magnitudes for the various source types by extrapolating from the J magnitudes using V J, V L, and V M stellar colors from Johnson (1966).
- g) The conversion from magnitudes to fluxes was done in a manner consistent with the absolute calibration of the DIRBE data (see COBE DIRBE Explanatory Supplement, 1997). The intensities of the FSM at 2.2 μ m were multiplied by a factor of 0.963 to account for differences between the color corrections of Sirius (which was used as the DIRBE

absolute calibrator) and those of K and M giants which dominate the emission of the FSM and have a CO absorption band partially within the 2.2 μ m DIRBE passband. There exist uncertainties of 10 – 15% in the model arising from details of the absolute calibration of the model and the differences and treatment of the various broadband filter responses (Cohen 1993b).

To check our FSM, we compared the results of our calculations to the average surface brightnesses of 238 large zones covering the entire sky as calculated by the SKY model (Cohen 1994b; see Table 7 of Wainscoat et al. (1992) for the zone boundaries). Our Faint Source Model reproduces the mean intensities calculated with the SKY model to within \sim 5% for most of the zones. The zones that are not well matched are all low-latitude zones below $|b| = 20^{\circ}$ (except for the zone containing the LMC and another near the Taurus region) which have been adjusted in the SKY model, but not in the FSM, for various localized features within the Galaxy (Cohen 1994a).

We have also compared the star counts expected from our FSM with the star counts from the prototype 2MASS survey in 7 fields at J and K_S (Skrutskie 1996). The fields are all in the first Galactic quadrant and span the range $8^{\circ} < b < 87^{\circ}$. The FSM star counts resemble the 2MASS star counts, although about half the fields show statistically significant differences, mostly at magnitudes J > 12 and $K_S > 12$. However, these fainter stars contribute a small enough fraction of total emission from these fields that the integrated brightnesses of the stars in the 2MASS fields are consistent with the predictions of the Faint Source Model. This comparison is limited by the small size of the fields $(0.12 - 7 \text{ deg}^2)$ and thus the large statistical uncertainties on the star counts.

Figure 3 shows the 2.2 μ m sky brightness calculated with the FSM. The model predicts the mean intensity in each pixel, and thus varies smoothly over the sky. The actual sky is not expected to be as smooth as the model because random Poisson deviations from the mean number of stars/magnitude in each pixel create intensity fluctuations. Faint discontinuities in the model are caused by the artificially sharp edges of the spiral arms, as defined in the model (Wainscoat et al. 1992; Cohen 1994a).

Maps of the FSM intensities at $1.25-25~\mu m$ can be obtained from the NSSDC COBE homepage website at http://www.gsfc.nasa.gov/astro/cobe/cobe_home.html.

4.3. The Residual Emission

Figure 4 shows the 1.25 – 4.9 μ m residual emission ($I_{ZG_S} \equiv I_{obs} - Z - G_S$) after the removal of stars and other compact objects with the bright source blanking and subtraction

of the FSM. At these wavelengths, the subtraction of the stellar emission is very effective at removing the brightness gradients at high Galactic latitudes. The maps are mottled by the emission of the remaining faint, marginally resolved stars, which lie below the bright source threshold. The average emission of these remaining stars is included in the smooth Faint Source Model. Therefore, over sufficiently large regions this stellar confusion acts as an additional noise term in the residual maps. At wavelengths $\leq 3.5~\mu m$ and low Galactic latitudes ($|b| < 10^{\circ}$), the FSM tends to overestimate the actual sky brightness, leading to negative residuals. A longitudinally anti-symmetric residual is present at the location of the Galactic bulge (most clearly seen in the 4.9 μm map of Fig. 4), which suggests that improvements could result if a bar-like model were used for the bulge (e.g., Dwek et al. 1995; Blitz & Spergel 1991). Some relatively large differences between the model and the data are found at locations where our implementation of the Faint Source Model has omitted particular adjustments for specific disk and spiral arm features (Cohen 1994a). Residual defects from the subtraction of the IPD emission are seen clearly at wavelengths $\geq 3.5~\mu m$ as S-shaped bands along the ecliptic.

In the mid-IR (after removal of IPD emission), the faint source emission contributes <40% of the observed brightness toward the inner Galaxy at low latitudes, and less than 5% and 1% for $|b| > 30^{\circ}$ at 12 and 25 μ m, respectively. The subtraction of the Faint Source Model in these bands is only apparent in the inner Galaxy, and residual intensity maps look nearly the same as those in Figure 1. The residual emission at wavelengths $\geq 12 \mu$ m is clearly dominated by the presence of ISM emission, $G_I(l, b, \lambda)$.

The FSM was not optimized to fit the DIRBE data, but is calculated from a fixed prescription based on a model designed to fit observed source counts in selected directions in the sky. It is therefore important to examine to what extent the removal of Galactic starlight with the FSM has under- or over-subtracted stellar emission from the maps. One test designed to look for such effects is to search for structure in the residual map that may be correlated with that of the FSM, or Galactic latitude.

Figures 5 and 6 illustrate the gradients of $I_{ZG_S}(l,b,\lambda)$ as a function of Galactic and ecliptic latitude, respectively, for the 1.25, 2.2, 3.5, and 4.9 μ m data. Table 1 lists the gradient and correlation coefficient for $I_{ZG_S}(l,b,\lambda)$ as a function of $\csc(|b|)$. The figures and table both show that the Faint Source model removes much of the Galactic gradient in the near-IR emission. Subtraction of the model also reduces the longitudinal variation of the near-IR sky brightness, as evidenced by the reduced dispersions at lower latitudes in Figures 5 and 6. At 4.9 μ m, the residual IPD gradient visible in Figure 6 is responsible for the structure in the residual emission as a function of $\csc(|b|)$ that is not observed at shorter wavelengths (Fig. 5).

5. Infrared Emission from the Galactic Interstellar Medium

The last foreground component we need to remove is the emission from the Galactic ISM. As outlined in Section 2, we use the 100 μ m DIRBE data (after removal of the IPD emission) to derive a spatial template of the ISM. We correlate the 100 μ m data with tracers of the gas phase of the ISM, and subtract emission that is uncorrelated with the ISM to form the 100 μ m ISM template. The external data used to trace the gas phase of the ISM are introduced in Section 5.1. Then we derive the 100 μ m emission per H I column density, and assess the possibilities that some of the emission comes from dust within the ionized and molecular phases of the ISM (§5.2). After subtracting the 100 μ m emission that is not associated with the ISM, we correlate the 100 μ m ISM template against the emission at other infrared wavelengths to derive the ISM intensity at those wavelengths (Section 5.3). The remaining subsections describe modified procedures that we apply to identify the ISM emission at the longest (240 μ m) and shortest (3.5 and 4.9 μ m) wavelengths.

The 100 μ m map is chosen as the template of the high latitude ISM because: (a) it provides full sky coverage; (b) it has better sensitivity than the maps at longer wavelengths where noisier bolometric detectors were used; (c) it is less affected by errors in the removal of IPD emission than the shorter wavelength maps; and (d) it represents a compromise between potential differences in spatial structure of the shorter and longer wavelength ISM emission. One drawback to this choice is that larger and a greater number of corrections for instrument temperature, charged particle radiation, and photon induced responsivity changes were required at 100 μ m than at any other wavelength (see *COBE* DIRBE Explanatory Supplement 1997).

5.1. External Data Sets

In order to identify that portion of the 100 μ m intensity (remaining after subtraction of IPD emission) that arises from the ISM, we need to compare the DIRBE data with other data sets that can be safely assumed to trace only Galactic ISM emission.

5.1.1. H I Data

Three H I 21 cm line surveys have been used for comparison with the long wavelength DIRBE data. The first is the AT&T Bell Laboratories survey of the sky north of $\delta = -40^{\circ}$ at an angular resolution of about 2° (Stark et al. 1992). The velocity-integrated ($|v| \leq 327$ km s⁻¹) line intensities were converted to H I column densities assuming the line emission is

optically thin, and a map of column density was produced in COBE sky-cube format (COBE DIRBE Explanatory Supplement 1997). The Bell Laboratories 20 foot horn reflector has very low far-sidelobe response. Lockman, Jahoda, and McCammon (1986) estimated that the maximum far-sidelobe contribution to observed column density is 8×10^{18} cm⁻², and the typical contribution is $0.5 \times 10^{18} \ \mathrm{cm}^{-2}$. The second data set consists of observations of an $8^{\circ} \times 9^{\circ}$ region centered on the North Ecliptic Pole $(l = 96^{\circ}, b = +30^{\circ})$ at 21' resolution (Elvis, Lockman, and Fassnacht 1994). Elvis et al. used the Bell Laboratories survey to correct their spectra for stray radiation, and estimated that the 1σ random error in column density is 1×10^{19} cm⁻². The third data set covers a 300 deg² region in Ursa Major surrounding the direction of lowest H I column density $(l = 150^{\circ}, b = +53^{\circ})$ at a resolution of 21' or better (Snowden et al. 1994). Snowden et al. also corrected their spectra for stray radiation, and estimated 1σ errors ranging from 0.5×10^{19} cm⁻² to 1.0×10^{19} cm⁻². Velocity-integrated maps of the North Ecliptic Pole and Ursa Major regions were obtained from F. J. Lockman (private communication). The velocity ranges of -150 to 150 km s⁻¹ for the North Ecliptic Pole and -150 to 100 km s^{-1} for Ursa Major include all significant Galactic emission. The maps were degraded to DIRBE resolution and reprojected to COBE sky-cube format.

5.1.2. CO Data

The CO data used in this analysis comprise the 12 CO survey of the Ophiuchus region by de Geus et al. (1990), and the 12 CO surveys of the Polaris flare, Ursa Major, and Camelopardalis regions by Heithausen et al. (1993). These surveys, which cover a total area of 900 deg² at high ($|b| > 15^{\circ}$) Galactic latitude, were taken with the 1.2 m millimeter-wave telescope initially located at Columbia University in New York City, and later at the Harvard-Smithsonian Center for Astrophysics in Cambridge, MA, or the nearly-identical Columbia Southern Millimeter-Wave Telescope in Cerro Tololo, Chile. Both telescopes have an angular resolution of 8.7 at the 12 CO J=1 \rightarrow 0 line frequency observed. The surveys were used to produce a velocity-integrated 12 CO map degraded to the resolution of the Bell Labs H I survey.

5.1.3. H II Data

The analysis presented in the Appendix makes use of pulsar dispersion measures from Taylor, Manchester, and Lyne (1993) and Camilo and Nice (1995), and H α intensities observed by Reynolds (1980, 1984, 1985, 1991b) using a Fabry-Perot spectrometer with a

beam 50' in diameter.

5.2. Correlation of 100 μ m Intensity with Gas Phases of the ISM

Our primary identification of the 100 μ m ISM emission is made through correlation with H I column densities toward the North Ecliptic Pole and the region of minimum H I column density (the Lockman Hole). The choice of these locations is determined by the low column densities, the availability of high quality H I data sets, and the ability to estimate or limit contributions from the molecular and ionized components of the ISM. The slope of the correlation is the average 100 μ m emissivity per H I column density. The intercept of the correlation is the mean intensity that is *not* associated with the H I component of the ISM. We also estimate the intensity of 100 μ m emission that may be associated with the ionized and molecular phases of the ISM. However, direct correlations between the 100 μ m emission and combinations of $N({\rm H~I})$ and $N({\rm H~II})$ or $N({\rm H_2})$ are found to be relatively ineffective because of low column density and/or emissivity of the molecular and ionized components.

5.2.1. Emission from Dust in H I

To determine the association of the 100 μ m emission with the neutral atomic ISM, we correlate the H I column density, N(H I), against the 100 μ m intensity after subtraction of IPD emission (and, in principle, any stellar emission), $I_{ZG_S}(100 \ \mu\text{m})$,

$$\nu I_{ZG_S}(100 \ \mu\text{m}) = A \ N(\text{H I}) + \nu I_0(100 \ \mu\text{m})$$
 (4)

to solve for the emissivity of the neutral ISM, A, and the mean intensity of emission that is uncorrelated with H I, $\nu I_0(100~\mu\text{m})$. Figure 7a shows the pixel-by-pixel comparison for the $8^{\circ} \times 9^{\circ}$ region centered on the North Ecliptic Pole (NEP). Figure 7b shows the comparison for the 300 deg² region surrounding the region of lowest H I column density (the Lockman Hole). Figure 7c shows the comparison for a region at $|b| > 25^{\circ}$, $|\beta| > 25^{\circ}$, and declination $\delta > -40^{\circ}$, using 100 μ m data smoothed to the resolution of the Bell Laboratories survey. This very large region is included to provide an indication of the extent to which the Lockman Hole and NEP regions are typical of other high latitude regions. Data in a 3 × 3 DIRBE pixel patch centered on the source RAFGL 5429 were excluded from Figure 7a, and data in 3 × 3 pixel patches around five galaxies (NGC 3079, 3310, 3556, 3690, and 4102) were excluded from Figure 7b. The solid lines show linear fits to the data that minimize χ^2 calculated using measurement errors in both variables (Press et al. 1992). Each plot shows

excess 100 μ m emission at the highest H I column densities. These data were excluded from the fitting by rejecting all data above a cut line that is perpendicular to the fit line on a plot where each variable is divided by its mean measurement error. The adopted cut lines are shown as short diagonal lines in Figures 7a-c. The cut line intersects the fit line at $N({\rm H~I})=5.0\times10^{20}~{\rm cm^{-2}}$ for the NEP region, at $1.5\times10^{20}~{\rm cm^{-2}}$ for the Lockman Hole region, and at 3.0×10^{20} cm⁻² for the region of Figure 7c. Each fit was done iteratively until the fit parameters and the data excluded by the cut stopped changing. The derived intercept values are not sensitive to the exact location of the cut lines. For the Lockman Hole region, for example, the derived intercept varied by less than $0.7~\mathrm{nW}~\mathrm{m}^{-2}~\mathrm{sr}^{-1}$ for a series of test fits in which the location of the cut line intersection ranged from 1.0×10^{20} to 2.0×10^{20} cm⁻². Figure 8 shows a comparison of the fit line with data averaged within uniformly spaced bins along the fit line for each of the three regions. In each region, the bin-averaged data are consistent with a linear relation over the range of column density used for the fitting. These correlations begin to deviate from linearity at higher column densities because of the contribution of emission from dust associated with molecular H₂ (e.g. Reach, Koo, & Heiles 1994; Reach, Wall, & Odegard 1998).

The fit parameters (slopes, A, and intercepts, $\nu I_0(100 \ \mu\text{m})$) are listed in Table 2. The tabulated uncertainties are formal errors determined from the 68% joint confidence region in parameter space. The average of the intercepts for the NEP and Lockman Hole regions, 19.8 nW m⁻² sr⁻¹, was subtracted from the 100 μ m IPD-subtracted skymap to form the spatial template of 100 μ m ISM emission (see Section 5.3). The difference between the intercepts for the NEP and Lockman Hole regions is 5.0 nW m⁻² sr⁻¹. This value was adopted as the systematic uncertainty for the zero level of the template.

Sources of systematic error that may affect the zero level of the 100 μ m ISM template include errors in subtraction of the IPD emission and errors due to variations in 100 μ m emissivity per neutral H atom (the $\nu I_{ZG_S}(100~\mu\text{m})/N(\text{H I})$ ratio for emission originating from the Galaxy) within the NEP or Lockman Hole regions. The latter could be caused by variations in dust temperature, grain composition, grain size distribution, or dust-to-gas mass ratio within the neutral atomic gas phase, or by emission from dust associated with ionized or molecular gas. If the 100 μ m emissivity per neutral H atom increases with increasing H I column density within a region, the intercept of the linear $\nu I_{ZG_S}(100~\mu\text{m})$ – N(H I) fit would underestimate the zero level of the emission from the ISM, and if it decreases with H I column density the intercept would overestimate the zero level. However, such systematic variations would tend to produce nonlinear $\nu I_{ZG_S}(100~\mu\text{m})$ – N(H I) relations. A quadratic dependence might be expected for a cloud containing H₂ (e.g., Dall'Oglio, et al. 1985; Reach, Koo, & Heiles 1994), but specific functional forms are not predicted for other causes of variation in emissivity per neutral H atom. A

simple interpretation of the linear relations found for the NEP and Lockman Hole is that systematic variations of emissivity per neutral H atom with H I column density are not important at low H I column densities in these regions.

The difference between the intercepts found for the NEP and Lockman Hole regions can probably be attributed to error in subtraction of IPD emission. Evidence for this can be seen in Figure 9, which shows that a weak ecliptic latitude dependence remains in the 100 μ m data after subtraction of the IPD emission model. The figure shows a similar ecliptic latitude dependence for data within four narrow ranges of H I column density. The intensity difference between $\beta=45^{\circ}$ and 75° in Figure 9 is comparable to the difference in intercepts derived for the Lockman Hole ($\beta=45^{\circ}$) and NEP ($\beta=90^{\circ}$).

5.2.2. Possible Emission from Dust in H II

Because the preceding correlations only identify the 100 μ m emission that is correlated with the neutral H I phase of the ISM, we need to estimate any error in the inferred zero level of the 100 μ m ISM template that may be caused by dust emission associated with the ionized phase of the ISM. The exact distributions of ionized hydrogen column density within the NEP and Lockman Hole regions are not known. However, for the Lockman Hole, available data can be used with some assumptions to estimate the possible error of the zero level. We initially assume that the 100 μ m emissivity per H nucleus within the H II gas phase equals the slope of the $\nu I_{ZG_S}(100~\mu\text{m}) - N(\text{H I})$ relation, and that the H II column density is constant within the region. Under these assumptions, the $\nu I_{ZG_S}(100~\mu\text{m}) - N(\text{H I})$ relation would still be linear but its intercept (I_0) would overestimate the zero level of emission from the ISM by N(H II) times the emissivity per H nucleus.

Table 3 lists information on ionized H column density for the Lockman Hole based on a pulsar dispersion measure and two H α observations. We are not aware of any useful data on ionized gas in the NEP region. The dispersion measure $DM \equiv \int n_e ds$ of PSR J1012+5307 provides a lower limit to the total $N({\rm H~II})$ along the line of sight. Estimates of the distance of the pulsar from the midplane are $z{=}460$ pc from photometry of its companion, assuming it is a $0.15M_{\odot}$ white dwarf (Lorimer et al. 1995; Halpern 1996), and $z{=}400$ pc from the dispersion measure and the Galactic electron density model of Taylor & Cordes (1993). Estimates of the exponential scale height of the ionized medium in the vicinity of the Sun range from 670 to 910 pc (Reynolds 1991a; Nordgren, Cordes, & Terzian 1992; Taylor & Cordes 1993). If the ionized gas in the Lockman Hole region has an exponential z distribution with a scale height in this range, and the pulsar is at $z{=}460$ pc, the total $N({\rm H~II})$ in the direction of the pulsar would be 2 to 2.5 times the dispersion

measure, or about 0.6×10^{20} cm⁻².

The H\$\alpha\$ observations provide a measure of \$\int T^{-0.92}n_e^2 ds\$ (e.g., Reynolds 1992), since extinction is negligible for lines of sight with such low H I column densities. H II column densities have been estimated from the H\$\alpha\$ data in Table 3 using a conversion factor of \$I(\text{H}\alpha)/N(\text{H II})=0.75\$ Rayleighs/10\$\frac{20}{20}\$ cm\$^{-2}\$ (1 Rayleigh = 10\$^6/4\$\pi\$ photons s\$^{-1}\$ cm\$^{-2}\$ sr\$^{-1}\$ = 0.24 nW m\$^{-2}\$ sr\$^{-1}\$ at \$H\$\alpha\$). This value was adopted based on the comparison of \$H\$\alpha\$ and dispersion measure data shown in Figure 10 for high \$|z|\$ pulsars. The figure shows that \$I(\text{H}\alpha)/DM\$ may increase with increasing H I column density. The \$I(\text{H}\alpha)/DM\$ ratio at the lowest H I column densities in the figure was adopted as the conversion factor for the Lockman Hole data. The adopted value corresponds to a characteristic electron density, \$n_c \equiv \int n_e^2 ds/\int n_e ds\$, of 0.05 cm\$^{-3}\$ for an electron temperature of 8000 K. For comparison, Reynolds (1991a) found a mean \$n_c\$ of 0.08 cm\$^{-3}\$ for lines of sight toward pulsars in 4 globular clusters at \$|z| > 4\$ kpc.

The $N({\rm H~II})$ values estimated from the H α observations are comparable to or smaller than the pulsar's dispersion measure. Even though we consider the $N({\rm H~II})$ estimates from the H α data to be more reliable than that derived from the dispersion measure, pulsar z distance, and scale height of ionized gas, to be conservative we adopt an intermediate value of $N({\rm H~II}){=}0.4{\times}10^{20}~{\rm cm}^{-2}$ as representative of the Lockman Hole region. Dust associated with ionized gas at this column density would have a 100 μ m intensity of 7 nW m⁻² sr⁻¹ under the assumptions described above, and the $\nu I_{ZG_S}(100~\mu{\rm m}) - N({\rm H~I})$ intercept I_0 would overestimate the zero level of the ISM emission by this amount, about 1/3 of the total.

However, this error estimate is probably too large, for two reasons. (1) The analysis presented in the Appendix suggests that the diffuse ionized gas at high galactic latitudes has a 100 μ m emissivity per H nucleus that is smaller than that of the H I gas. A 3σ upper limit of 3/4 times the emissivity per H nucleus of the H I gas was found for a $10^{\circ} \times 12^{\circ}$ region at $l=144^{\circ}$, $b=-21^{\circ}$. Analysis by Fixsen et al. (1998) using COBE/FIRAS data also indicates that the emissivity of the ionized gas is small. They correlate far-IR emission against a combination of [C II] line emission, as a tracer of the ionized ISM, and linear and quadratic H I column density, as a tracer of the neutral ISM. At high latitudes, they find little or no far-IR continuum emission correlated with the [C II] line emission. (2) It is likely that H II column density is not constant in the Lockman Hole region, but is correlated to some degree with H I column density. Such correlations are found in the Appendix for data along lines of sight toward two samples of high |z| pulsars. If such a correlation exists in the Lockman hole, the error estimate for the 100 μ m zero point should be calculated using only the component of N(H II) that is not correlated with N(H I).

Further evidence for correlation between ionized and atomic gas has been shown for the $10^{\circ} \times 12^{\circ}$ region at $l = 144^{\circ}$, $b = -21^{\circ}$ by Reynolds et al. (1995). They found that at least 30 percent of the total H α emission and 10 to 30 percent of the total 21 cm line emission are kinematically and spatially associated in clouds containing both neutral and ionized gas. For these reasons, we adopt 4 nW m⁻² sr⁻¹, about 1/5 of the total, as the maximum possible systematic error in the zero level of the 100 μ m ISM template that may result from H II associated dust.

5.2.3. Possible Emission from Dust in H_2

We additionally need to estimate the error in the zero level of the 100 μ m ISM template that may be caused by emission from dust associated with the molecular ISM. Table 3 lists 3-sigma upper limits on H_2 column density for both the Lockman Hole and NEP regions, based on upper limits to ^{12}CO J=1-0 line emission within a $10^{\circ} \times 10^{\circ}$ portion of the Lockman Hole region and toward some H I emission peaks in the NEP region. [CO emission has been detected toward the 100 μ m brightness peaks of a few cirrus clouds elsewhere in the Lockman Hole region by Heiles, Reach, & Koo (1988), Stacy et al. (1991), and Reach, Koo, & Heiles (1994). The H I column densities at these positions are 1.9×10^{20} cm⁻² or greater, so they were excluded from the $\nu I_{ZG_S}(100 \ \mu \text{m})$ vs. N(H I) fitting.] Following Elvis et al. (1994), limits on observed line emission were converted to limits on H₂ column density assuming a 1 km $\rm s^{-1}$ line width, typical of diffuse clouds, and a CO intensity to $N(\rm H_2)$ conversion ratio of $X_{CO} < 4 \times 10^{20} \text{ mol cm}^{-2} \text{ (K km s}^{-1})^{-1}$. Most determinations of X_{CO} for translucent molecular clouds (clouds with visual extinction in the range $1 < A_V < 5$ mag) are consistent with this upper limit (Magnani & Onello 1995, and references therein). Dust associated with molecular gas at or below the $N(H_2)$ limits in Table 3 would produce 100 μm intensities of <42 and <23 nW m⁻² sr⁻¹ for the Lockman Hole and NEP, respectively, assuming constant $N(H_2)$ across these regions and emissivity per H nucleus equal to the slope of the $\nu I_{ZG_S}(100 \ \mu\text{m})-N(\text{H I})$ relation. These conclusions for the Lockman Hole and NEP can be extended to cover the entire north Galactic hemisphere, since a recent CO survey for $b \ge 30^{\circ}$ by Hartmann, Magnani, & Thaddeus (1998) has comparable sensitivity to the measurements in Table 3 and finds that detectable CO has a filling factor of 0.004 – 0.006.

For the Lockman Hole region, the H_2 column density and the possible 100 μ m emission from dust associated with H_2 are probably much smaller than allowed by the limit on CO line intensity. Ultraviolet absorption line observations toward early type stars have shown that a transition in the fraction of H in molecular form occurs at color excess

 $E(B-V) \simeq 0.08$ mag, or at $N({\rm H~I}) + 2N({\rm H}_2) \simeq 5 \times 10^{20}$ atoms cm⁻², above which more than 1% of H atoms are in the form of H₂ (Savage et al. 1977). Studies of the H I–H₂ phase transition based on H I, CO, and 100 μ m observations of high latitude molecular clouds are consistent with this (Reach, Koo, & Heiles 1994; Gir, Blitz, & Magnani 1994). The $N({\rm H}_2)$ limit in Table 3, together with the maximum H I column density used in the $\nu I_{ZG_S}(100 \ \mu m) - N({\rm H~I})$ fitting, yields $N({\rm H~I}) + 2N({\rm H}_2) < 4.0 \times 10^{20}$ atoms cm⁻², suggesting that the gas in the Lockman Hole is below the threshold for significant fractional H₂ abundance. However, the $N({\rm H}_2)$ limit may not be valid if H₂ is present in clouds that are too diffuse for CO to exist.

Estimates of visual extinction toward the Lockman Hole give another indication that the H₂ column density is very low. The Galactic reddening map of Burstein & Heiles (1982), which is based on maps of galaxy counts and H I column density and is calibrated using reddening measurements for globular cluster stars and RR Lyrae stars, gives a mean E(B-V) of -0.006 ± 0.01 for the Lockman Hole region. The reddening map of Holmberg (1974), based on counts of distant Zwicky galaxy clusters and calibrated assuming A_B =0.25 at the galactic poles, gives $E(B-V) = 0.035 \pm 0.014$. The difference between these results is primarily due to differences in calibration; if the Holmberg map were recalibrated to the mean polar reddening of Burstein and Heiles, the results would agree within the quoted relative errors. Recent determinations of polar absorption by different methods are in the range $0 < A_B < 0.21$ (de Vaucouleurs 1995; Knude 1996, and references therein) so the mean E(B-V) for the Lockman Hole region is probably less than 0.035 and the reddening for most or all of the positions used for the $\nu I_{ZG_S}(100 \ \mu\text{m})-N(\text{H I})$ fitting is probably below E(B-V) = 0.08. Adopting the largest fractional H₂ abundance measured by Savage et al. (1977) for E(B-V) < 0.08 would give an average H₂ column density of 5×10^{15} mol ${\rm cm}^{-2}$ for the Lockman Hole. Assuming constant $N({\rm H}_2)$ within the region and emissivity per H atom in the H₂ phase equal to the slope of the $\nu I_{ZG_S}(100~\mu\mathrm{m})$ – $N(\mathrm{H~I})$ relation, dust associated with molecular gas would give rise to a 100 μ m intensity of only 0.002 nW ${\rm m}^{-2}~{\rm sr}^{-1}$.

As in the case for the ionized ISM, we have also attempted to determine the 100 μ m emissivity of the molecular ISM. For each of the four regions covered by the above ¹²CO surveys (§5.1.2), we performed a least-squares fit of the equation

$$\nu I_{ZG_S}(100 \ \mu\text{m}) = A \ N(HI) + B \ W(CO) + \nu I_0(100 \ \mu\text{m}) \tag{5}$$

to the data by varying the parameters A, B, and νI_0 , where A is the 100 μ m emissivity per H atom for the H I gas phase, B is the product of the 100 μ m emissivity per molecule for the H₂ gas phase and the ratio of H₂ column density to ¹²CO intensity, and νI_0 represents any background emission. In each case the resulting fit to the 100 μ m fluxes is significantly

poorer than those obtained in Figure 7, where the contribution of dust associated with molecular gas to the 100 μ m emission is believed to be negligible. The breakdown of the infrared-gas column density correlation within high-latitude regions having significant CO emission may result from one or more of the following: (1) There may be a greater variability in the dust-to-gas mass ratio or dust temperature within H₂ regions than within H I regions; (2) Regions with a higher CO content may have more dust associated with ionized gas which is not accounted for in the correlations. The photographic H α survey of Sivan (1974) shows that a significant fraction of the Ophiuchus region contains extended H II regions; (3) The dust column density within these regions may be too low to effectively shield the CO molecule from dissociating UV radiation (see, for example, Heithausen et al. 1993), and therefore the velocity-integrated ¹²CO intensity may not accurately trace the H₂ column density along the line of sight.

5.3. Correlation of the Other DIRBE Bands with the 100 μ m Emission

Having estimated the 100 μ m emission that is not associated with the ISM ($\nu I_0 = 19.8$ nW m⁻² sr⁻¹), we construct the $G_I(l,b,100~\mu\text{m})$ map from $I_{ZG_S}(l,b,100~\mu\text{m}) - I_0(100~\mu\text{m})$, which is then used as the template for the ISM emission for derivation of maps of the background emission at the other DIRBE wavelengths:

$$I_0(l, b, \lambda) = I_{ZG_S}(l, b, \lambda) - R(\lambda)G_I(l, b, 100 \ \mu \text{m}).$$
 (6)

We fit the correlations of I_{ZG_S} to G_I to determine $R(\lambda)$, the $\lambda - 100 \ \mu \text{m}$ color, from the slope of the correlation and a mean $I_0(l,b,\lambda)$ from the intercept. These correlations and associated least-squares fits are shown in Figure 11. The slopes and their statistical uncertainties are given in Table 4. For the far-IR bands, the correlations are determined only for the regions where $|b| > 45^{\circ}$. Using a cut at lower latitudes resulted in a steeper slope, influenced by bright clouds found only at the lower latitudes. A higher latitude cut resulted in a shallower slope, possibly an artifact of the poorer correlation provided by the fainter, very high latitude cirrus. We settled on the 45° cut as a compromise between the weaker correlations at higher latitudes, and the intrinsic color temperature variations between the clouds visible at the lower latitudes. At mid-IR wavelengths, residuals for the IPD removal (Paper II) were too large to allow use of this entire region for correlation. Smaller regions where the IPD and FSM removal have left no obvious structure were used: $|b|>30^{\circ}$ and $|\beta|>40^{\circ}$ at 60 $\mu{\rm m}$, and $\beta>70^{\circ}$ at 12 and 25 $\mu{\rm m}$. In the near-IR bands $(\lambda \leq 4.9 \ \mu \text{m})$, residuals from removal of starlight and IPD scattering and emission were too large to allow a direct correlation of these bands with the 100 μ m ISM template (see Section 5.5).

In using linear least-squares fits, it is assumed that the $R(\lambda)$ colors of the ISM are constant at high latitudes. The validity of this assumption is indicated by relatively large correlation coefficients, and by dispersions about the least-squares fit relation which are no more than a factor of 2 greater than those expected from the uncertainties associated with the IPD-subtracted data. These quantities are listed in Table 4. Another indication of the expected uniformity of the $R(\lambda)$ colors is the observed Galactic temperature gradient reported by Sodroski et al. (1994). Even though this radial temperature gradient leads to large color variations at low latitudes, at $|b| > 45^{\circ}$ the gradient implies large scale variation in the R(240) color of only $\pm 4\%$ between the inner and outer Galaxy. The color variations at other wavelengths should be even smaller, as the radial temperature gradients are smaller (Sodroski et al. 1987, 1989). In our present results any such large scale trends are obscured by smaller scale cloud-to-cloud variations and therefore have no direct impact on the derived background level.

Scaling the 100 μ m ISM template by the appropriate colors ($R(\lambda)$ from Table 4) and subtracting it from each of the mid- and far-IR wavelength maps yields the maps shown in Figure 12. For the 100 μ m residual map we depict the subtraction of 1.84×10^{-19} nW m⁻² sr⁻¹ cm² × N(H I) from the data (derived in Section 5.2.1). These maps show the end result of our removal of both IPD and Galactic emission. They should contain the full CIB signal as well as any residual emission left by imperfect foreground modeling. Figures 13 and 14 illustrate the gradients depicted in the residual sky brightness of these maps as functions of Galactic and ecliptic latitude. Table 5 lists these gradients and the correlation coefficients with respect to csc(|b|). At 12 and 25 microns, the subtraction of the ISM emission allows the residual gradients of IPD emission to be seen and characterized more clearly, as indicated by Figures 12, 13, and 14 and in Table 5. At longer wavelengths, the IPD residuals are weak compared to the residual ISM emission.

5.4. A Two-Component Model for the 240 μ m Emission

The single component model of the ISM based on the 100 μ m data removes much of the emission of the ISM at high latitudes. However the residual maps (Fig. 12) show that at the far-IR wavelengths a strong second component to the ISM emission is still present, especially at lower latitudes ($|b| < 30^{\circ}$). The similarity of the 140 and 240 μ m residual maps suggests that a two-component model with templates formed from the 100 μ m ISM emission and the 140 μ m residual could be effective at removing the 240 μ m emission of the ISM. For a linear combination of these two templates, we can substitute an equivalent linear combination of the 100 μ m ISM emission and the 140 μ m ISM emission. We use a

linear least squares fit to solve for the coefficients that scale the templates to fit the 240 μ m data. Performing this correlation over the entire unblanked sky leads to a 240 μ m ISM model of

$$G_I(l, b, 240 \ \mu\text{m}) = -1.702G_I(l, b, 100 \ \mu\text{m}) + 1.555G_I(l, b, 140 \ \mu\text{m}), \tag{7}$$

where the ISM components at 100 and 140 μ m have had constant terms (estimated from the one-component ISM subtraction residuals) of 19.8 and 18.5 nW m⁻² sr⁻¹ removed respectively. This two-component model of the ISM emission will be referred to as the "ISM2" model to distinguish it from the one-component (ISM1) model described in §5.3.

A map of the residuals after subtraction of the ISM2 model from the data is shown in Figure 15. The residuals are plotted as functions of Galactic and ecliptic latitude, b and β , in Figs. 13 and 14. This model appears to do an excellent job at removing the ISM emission variation all the way down to $b \sim 0^{\circ}$. The increase in noise in the residual map occurs as a result of the introduction of the noisy 140 μ m data as part of the model. The noise partially obscures some deficiencies in the residual map, such as some remaining emission from the IPD which can be seen in a wide band along the ecliptic. This residual emission arises primarily from the incomplete subtraction of IPD emission at 100 μ m.

Physically, the ISM2 model subtraction works well because it allows us to account for both the large-scale and local temperature variations of the interstellar dust. This is demonstrated by noting that the coefficients in Equation 7 define a line in the $100 - 140 - 240 \mu \text{m}$ color-color plot (Fig. 16). This line is a good representation of the data, which are distributed along a nearly linear trend because of temperature variations in the ISM. The bright source blanking (Section 4.1) has removed the hottest sources (mostly H II regions) which would extend the range of the data in the color-color plot, but with a distinctly nonlinear trend. Only high signal-to-noise data ($\nu I_{ZG_S} > 1200 \text{ nW m}^{-2} \text{ sr}^{-1}$) were used in constructing Figure 16, therefore small errors in the zero levels of each band will have little effect on the colors. However, the gain uncertainties (§6.1 and Table 6) are large enough to cause systematic changes in the colors. Gain errors of $\sim 7\%$ in each color would cause the displacement between the observed colors and the expected color trend for blackbodies with emissivities $\sim \nu^2$.

5.5. Near-IR Intensities

For the near-IR wavelengths, the subtraction of the starlight is not sufficiently accurate to yield values of $R(\lambda)$ and $I_0(l, b, \lambda)$ from direct correlations of the near-IR data with $G_I(l, b, 100 \ \mu\text{m})$. The 1.25 – 4.9 μ m emission maps in Figure 4 show little similarity to

the 100 μ m emission maps in Figure 1. Therefore, to determine the intensity of the ISM emission at these wavelengths we make use of the color differences between the starlight and the ISM emission, as revealed in the IPD-subtracted maps $(I_Z \equiv I_{obs} - Z)$. Colors formed from the simple ratio of two near-IR intensities, e.g. $I_Z(l, b, 1.25 \ \mu\text{m})/I_Z(l, b, 2.2 \ \mu\text{m})$, can reveal extinction effects as well as intrinsic source variations. We remove the influence of extinction by using the reddening-free parameter:

$$Q(1.25, 2.2, 3.5) = [I_Z(1.25)/I_Z(2.2)]^{\zeta}/[I_Z(2.2)/I_Z(3.5)]$$
(8)

where

$$\zeta = (A_{2.2}/A_{1.25} - A_{3.5}/A_{1.25})/(1 - A_{2.2}/A_{1.25}) \tag{9}$$

and $A_{\lambda}/A_{1.25}$ is the ratio of extinction at wavelength λ to that at 1.25 μ m. The ratio of absorption coefficients is calculated from the extinction law of Rieke & Lebofsky (1985), which has been shown to match the inner Galaxy extinction seen by DIRBE (Arendt et al. 1994).

The reddening-free parameter is constructed to be independent of the amount of extinction; it only varies if the sources of emission vary. In fact, Q(1.25, 2.2, 3.5) is fairly insensitive to stellar spectral type, so the bulk of the stellar emission of the Galaxy can be characterized by a single value, $Q_0(1.25, 2.2, 3.5)$. Thus, variations in Q(1.25, 2.2, 3.5) will be observed where there is significant *emission* from hot interstellar dust. The map of Q(1.25, 2.2, 3.5) (in Figure 17) does show more structure of the ISM at low latitudes than do the near-IR intensity maps of Figure 4, though residual IPD emission still obscures high latitude structure.

Based on the observation that the $I_Z(l, b, 1.25 \ \mu\text{m})/I_Z(l, b, 2.2 \ \mu\text{m})$ map shows little or no evidence of diffuse ISM features at $|b| \gtrsim 10^{\circ}$, while the $I_Z(l, b, 2.2 \ \mu\text{m})/I_Z(l, b, 3.5 \ \mu\text{m})$ map shows such features clearly, we assume the ISM emission is only significant at 3.5 μ m, i.e.

$$I_Z(1.25) = G_S(1.25) \tag{10}$$

$$I_Z(2.2) = G_S(2.2) (11)$$

and

$$I_Z(3.5) = G_S(3.5) + G_I(3.5).$$
 (12)

Then we can derive the ISM emission as

$$G_I(3.5) = I_Z(3.5) \times [1 - Q_0(1.25, 2.2, 3.5)/Q(1.25, 2.2, 3.5)].$$
 (13)

Rather than imposing a value of $Q_0(1.25, 2.2, 3.5)$, we can again use a linear least squares fit to derive $Q_0(1.25, 2.2, 3.5)$ and the near-IR cirrus color, R(3.5). We do this by

considering

$$R(3.5) \equiv G_I(3.5)/G_I(100) \tag{14}$$

$$= I_Z(3.5) \times [1 - Q_0(1.25, 2.2, 3.5)/Q(1.25, 2.2, 3.5)]/G_I(100)$$
 (15)

$$= \frac{Q(1.25, 2.2, 3.5) - Q_0(1.25, 2.2, 3.5)}{Q(1.25, 2.2, 3.5) \times G_I(100)/I_Z(3.5)}.$$
(16)

By rewriting this last equation as

$$Q(1.25, 2.2, 3.5) = R(3.5) \times [Q(1.25, 2.2, 3.5) \times G_I(100)/I_Z(3.5)] + Q_0(1.25, 2.2, 3.5)$$
(17)

we see that the color R(3.5) can be found as the slope of a least-squares fit of Q(1.25, 2.2, 3.5) vs. $[Q(1.25, 2.2, 3.5) \times G_I(100)/I_Z(3.5)]$. The intercept of the fit is $Q_0(1.25, 2.2, 3.5)$, the nominal stellar reddening-free parameter. In a nearly identical manner we can also derive the R(4.9) color of the ISM emission. Finally, having determined these near-IR colors, we can use them to scale and subtract the 100 μ m template of the ISM emission from the 3.5 and 4.9 μ m data.

Because of the very low intensity of the ISM in the near-IR relative to the residual errors of the IPD model, the correlations need to be done at low Galactic latitudes ($|b| < 30^{\circ}$). The correlations and corresponding least-squares fits are shown in Figure 18. The 3.5 and 4.9 μ m colors derived by this method are listed in Table 4. The statistical uncertainties in the determination of the 3.5 and 4.9 μ m colors are as good those for the far-IR wavelengths. The residual maps after subtraction of the derived near-IR emission are shown in Figure 12. (At 4.9 μ m, the residual IPD emission is also reduced because the 100 μ m ISM template contains some residual IPD emission as well.)

In this derivation of the near-IR emission there are two important assumptions. The first is that the near-IR emission of the ISM within the high-latitude regions of interest is similar to that which is measured at low latitudes by this procedure. The bright source blanking at low latitudes removes most of the compact emission sources (mainly H II regions) in the area where the ISM colors are derived. The remaining emission may still arise from ISM with different properties than those of the local high-latitude ISM, but the residual maps (Figure 12) give no indication of differences between the unblanked low and high latitude ISM emission. The second assumption is that any near-IR emission of the CIB can be neglected in this analysis. At the low galactic latitudes where the ISM colors are derived, stellar emission is likely to be much stronger than the CIB emission. Additionally, the slopes of the correlations, which indicate the ISM colors R(3.5) and R(4.9), should not be seriously affected by any isotropic emission, such as that of the CIB.

6. Uncertainties

The value of the foreground subtracted maps (Figure 12) as estimators of the CIB intensity depends upon of the uncertainties associated with the data and foreground models. We distinguish two classes of uncertainties. Random uncertainties, such as those arising from the detector noise, are associated with errors exhibiting Gaussian or Poisson statistics. In general, random uncertainties can be reduced by averaging large amounts of data (i.e. over large regions of the sky, and over the entire mission) and do not contribute significantly to the total uncertainty of the residual maps. Systematic uncertainties, such as those associated with the detector offsets, affect many or all data in a similar fashion and thus do not average out as the size of the data set increases. The following sections describe our estimates of the most significant systematic uncertainties associated with each step of the foreground removal process.

6.1. Instrumental Uncertainties

The calibration of the DIRBE data requires the measurement of instrument gain and offset terms. Errors in the measurement of these quantities will affect all data in a similar fashion. The evaluation of the gain and offset uncertainties is described in the COBE DIRBE Explanatory Supplement (1997). The uncertainties in the detector gains and offsets are listed in Table 6. Gain errors will have little impact on the significance of a detected background signal, because the IPD and ISM models are scaled directly to the DIRBE data. The FSM is not scaled to the DIRBE data directly, but does use the DIRBE absolute calibration for conversion from magnitudes to flux densities. A gain error will cause us to overstate or understate the levels of the residual signal and its total uncertainty by a multiplicative constant. The detector offset uncertainties are much more important. They represent minimum uncertainties that cannot be reduced. A true background signal must at least exceed the offset uncertainties to be detected. The detector offset uncertainties are worst for the 140 and 240 μ m bands.

After averaging over the entire mission, random instrumental noise is only apparent in the 140 and 240 μ m maps as a graininess visible at the fainter high latitudes. However, averaging over regions larger than ~ 30 pixels ($\approx 10^{-3}$ sr ≈ 3 deg²), reduces the uncertainty from the instrumental noise to levels below that of the total systematic uncertainties. At shorter wavelengths, the instrumental noise is dwarfed by the systematic uncertainties even on the scale of a single pixel.

6.2. Uncertainties of the IPD Model

The uncertainties and errors in the subtraction of the emission and scattered light from the IPD are reported in Paper II. Of these uncertainties, the one likely to be most significant is that arising from uncertainty in the geometry of the interplanetary dust cloud. The adopted geometric kernel does not uniquely or perfectly describe the data, and consequently we are required to associate systematic errors to the residual intensities that are roughly proportional to the mean intensity of the IPD at each wavelength. These uncertainties are listed in Table 6.

6.3. Uncertainties of the Faint Source Model

The systematic uncertainty associated with the removal of Galactic stellar emission has two sources. First, there is uncertainty associated with the bright source blanking. At some locations the blanking may remove confused sources which are individually below the bright source threshold, but are combined by the DIRBE beam into a single source above the threshold. The result of this effect is to reduce the mean level of the background when measured over large regions. We have used the Faint Source Model to estimate the frequency with which we expect to find pairs of sources in the same DIRBE pixel, where both sources are within a factor of 2 of the bright source threshold. The number of such double sources at latitudes $|b| > 30^{\circ}$ ranges from ~ 140 at 1.25 μ m to ~ 6 at 4.9 μ m. The uncertainties caused by these sources are listed in Table 6.

A more important source of systematic uncertainties in the removal of stellar foreground emission is the accuracy of the Faint Source Model. Systematic errors in the Faint Source Model are not strictly isotropic, but occur on large angular scales such that averages over large patches usually do not reduce the errors. The clearest indication of systematic errors in the Faint Source Model is the presence of gradients with respect to Galactic latitude in the residual emission at 1.25 to 4.9 μ m. The correlations between these gradients and the FSM at $|b| \gtrsim 30^{\circ}$ are used to derive the uncertainties reported in Table 6. The gradients indicate that low latitude emission is oversubtracted relative to the high latitude emission, but they cannot indicate at which latitude (if any) the subtraction is correct.

6.4. Uncertainties of the ISM Model

We have estimated two contributions to the uncertainty associated with the subtraction of the ISM. The first is the uncertainty of the background level that is removed from the 100 μ m map to make the ISM template (see Sections 5.2, 5.3). Any error in this value is propagated into the residual intensities measured at other wavelengths. The uncertainty in the 100 μ m background intensity is taken to be the difference in the intercepts of the correlations between the H I and 100 μ m emission at the NEP and at the Lockman Hole (Section 5.2.1), which were used to derive the 100 μ m background intensity. This uncertainty would be larger if we had determined the background using a larger region of the sky, where there would be stronger and less well known contibutions from molecular and ionized components of the ISM. The 100 μ m instrumental offset and IPD uncertainties are added in quadrature to this ISM uncertainty before the value is propagated to other wavelengths. The other ISM uncertainty is that associated with the scaling factors, $R(\lambda)$, used to convert the 100 μ m ISM emission into ISM emission maps at other wavelengths. These uncertainties were estimated by subdividing the region of sky used to determine $R(\lambda)$ into ~ 18 regions, and then calculating $R(\lambda)$ for each subregion. The rms variation of $R(\lambda)$ for the set of subregions was used as the uncertainty for the global $R(\lambda)$ applied in the ISM subtraction. This uncertainty characterizes the variations in the ISM spectrum on angular scales of $\sim 30^{\circ}$. Both of the systematic uncertainties associated with the ISM subtraction are listed in Table 6.

6.5. Total Uncertainties of the Residual Emission

After removal of the IPD and Galactic IR foregrounds, the total uncertainty attributed to the residual background intensity at each wavelength is calculated as the quadrature sum of the systematic uncertainties ($\sigma_{\text{total}} = \sqrt{\Sigma \sigma_i^2}$) discussed above and listed in Table 6.

7. Interpretations

7.1. Modifications to the Faint Source Model

In constructing the FSM, we attempted to reproduce the model described by Wainscoat et al. (1992) as closely as possible. This preserves the model's basis in source counts and independence from the actual intensity of the CIB. The only modification made to the model in order to improve its fit to the DIRBE data was the addition of an 18 pc offset of the Sun above the Galactic midplane. This value is supported by the independent results derived at near-IR wavelengths by Cohen (1995), and other analyses of the DIRBE data (Weiland et al. 1994; Freudenreich 1996) bracket the value used here. However, the final residual maps in the near-IR bands (Fig. 12), and the gradients with respect to Galactic

latitude (Table 5) clearly indicate that the FSM has overaccounted for the stellar emission.

This suggests the possibility of adjusting the FSM to minimize these gradients. The simplest adjustment would be to apply a global scaling factor to the model intensities. Such a factor could arise if there were an error in the flux attributed to 0–magnitude stars in the FSM. The scaling factors required to minimize the Galactic latitude gradients of the residual maps are 0.859, 0.792, and 0.674 at 1.25, 2.2, and 3.5 μ m, respectively. However, these adjustments are significantly larger than the $\sim 3\%$ gain uncertainties expected at these wavelengths (COBE DIRBE Explanatory Supplement, 1997). These scaling factors could also be attributed to errors in the absolute magnitudes of 0.165, 0.253, and 0.428 magnitudes for all source types at 1.25, 2.2, and 3.5 μ m, respectively. If these scaling factors are applied to the FSM, then the residual intensities at high Galactic latitude increase by factors of \sim 2 in all three bands.

Alternatively, we can use the star count data from the seven 2MASS fields to optimize the fit of the FSM to this independent data set. To minimize the χ^2 statistic for the comparison of the J and K band data simultaneously, we find that the FSM star counts (number of stars/mag/deg²) need to be reduced by a factor of 0.952 to match the 2MASS data. Such a change in the number density of stars in the FSM would eliminate about 1/2 of the gradient that is observed in the residual maps. Changes that optimize the fit to the 2MASS star counts do not simultaneously minimize the residual gradients in the DIRBE data.

None of these scaling changes were applied to either the intensities or the number densities of the stars in the FSM in the present analysis because we sought to keep the FSM tied closely to the star counts, and because we are unable to determine the physical cause of the apparent discrepancy between the FSM and the DIRBE data.

7.2. Implications for the ISM

The IR emissivity and colors of the ISM derived in this paper differ somewhat from those found in other analyses. Using the DIRBE data, but a different method for removing the IPD emission, Boulanger et al. (1996) find a 100 μ m emissivity of 15.9 nW m⁻² sr⁻¹ / 10^{20} cm⁻², which is about 15% lower than the average for the NEP and Lockman Hole regions (Table 2). Dwek et al. (1997) presented an analysis of an ISM spectrum that was derived in a similar manner to that presented in Table 4, but using an earlier version of the IPD emission removal than that used in this work (Paper II). The high latitude ISM spectrum presented here is considered an improvement on that presented by Dwek et al.

(1997), though differences are generally $\leq 10\%$ and within the adopted uncertainties.

Dwek et al. (1997) find that the ISM spectrum is well fit by emission from silicate grains, graphite grains, and PAHs, all heated by the mean interstellar radiation field. The near-IR emission ($\lambda \leq 12~\mu\text{m}$) provides strong evidence that the PAH abundance is higher than expected from most previous studies. The amount of carbon in graphite grains, PAHs, and as C⁺ ions is found to be consistent with cosmic abundances.

At 240 μ m the results of the two-component ISM model (ISM2) indicate that it is important for a model of Galactic IR emission to account for spatial variation in the dust temperature. The contrast between Figure 15 and Figure 12 shows this is especially relevant at low latitude ($|b| \lesssim 20^{\circ}$). However, because of the increased noise in the ISM2 model, it remains unclear how important temperature variation is at high latitudes. A two-component model, similar in form to the ISM2 model used here, is also required to model the Galactic emission observed by the COBE/FIRAS experiment (Fixsen et al. 1997). Another recent study using both DIRBE and FIRAS data (Lagache et al. 1998) decomposes the ISM emission into warm (~ 17.5 K) and colder (~ 15 K) components. The distribution of this cold component (Figure 5 of Lagache et al. 1998) is very similar to that of the 140 and 240 μ m residual emission after removal of the one-component ISM model (Figure 12). In this two temperature model, the apparent temperature variations revealed in the long wavelength colors are (at least in part) a result of varying proportions of the warm and colder ISM components on different lines of sight.

7.3. Inadvisable Estimates of the CIB

There are several numbers presented in this paper that should not be used as estimates of the CIB, despite their appearances. These include extrapolation of the $\csc(|b|)$ or $\csc(|\beta|)$ gradients discussed in Sections 4.3 and 5.3, intercepts of the correlations between $\nu I_{ZG_S}(100\,\mu\text{m})$ and N(H I) (and other ISM tracers) discussed in Section 5.2, and the intercepts of the correlations of other DIRBE intensity maps with the 100 μ m ISM template discussed in Section 5.3. The main reason these numbers are not reliable estimates of the CIB is that they are derived from regions chosen for characterization of the Galactic foreground, not for accuracy or completeness of removal of the Galactic and other foregrounds. Frequently these regions include entirely or in part areas where the Galactic emission is relatively strong, and small fractional errors in the foreground removal could still have large influences on the derived intensity of the CIB. A more useful investigation of the CIB should focus on regions of the sky where errors in the foreground removal have minimal impact on the derived CIB. A proper analysis of the CIB also needs a demonstration that the residual

emission is isotropic, rather than just providing a single intensity estimate that may average over anisotropic defects in the foreground removal. Such a study of the CIB is presented in Paper I. Any conclusions concerning the CIB should be drawn from that paper.

8. Conclusions

We have modeled and removed the Galactic IR emission in the DIRBE data in preparation for analysis of the CIB. The procedures used were designed to preserve the emission of the CIB in the residual maps, and not remove it inadvertently with the Galactic emission. The procedures concentrated on producing accurate results at high latitudes where Galactic emission is weakest. At low latitudes, deficiencies in the models are clearly visible in the residual maps.

We find that the stellar emission of the Galaxy is reasonably reproduced by our Faint Source Model, which is based on the SKY model (Wainscoat et al. 1992; Cohen 1993a, 1994a, 1995). An offset of the Sun by ~ 18 pc from the Galactic plane is required to produce equal residual near-IR intensities at north and south Galactic latitudes. However, there is clearly room for improvement in the geometry or calibration of the FSM.

We find that the ISM can be fairly well modeled by a single spatial and spectral component if we constrain our study to high Galactic latitudes. At 240 μ m, a model of the ISM with two spatial components can produce a much more complete subtraction of the ISM, extending to low Galactic latitudes. The two spatial components can combine to produce a range of color temperatures across the sky. This shows that a complete model of the ISM needs to be able to account for a continuous range of dust temperatures. We are unable to detect any IR emission associated with low density ionized gas at high Galactic latitudes.

The authors gratefully acknowledge the contributions over many years of the many engineers, managers, scientists, analysts, and programmers engaged in the DIRBE investigation. The National Aeronautics and Space Administration/Goddard Space Flight Center (NASA/GSFC) is responsible for the design, development, and operation of *COBE*. Scientific guidance is provided by the *COBE* Science Working Group. GSFC is also responsible for the development of the analysis software and for the production of the mission data sets.

H. T. Freudenreich is thanked for his work on developing and implementing the procedures used for blanking the bright sources (Section 4.1). We thank M. Cohen, who

provided results from the SKY model and technical assistance, which were very useful for the development of our Faint Source Model. We also thank M. Skrutskie, S. Price, R. Cutri, M. Egan, and others in the 2MASS project for making some of their prototype camera data available for this research.

The data described in this paper are available to the public through the NSSDC COBE homepage website at http://www.gsfc.nasa.gov/astro/cobe/cobe_home.html. The mission-averaged zodi-subtracted residual skymaps are contained in the 'Zodi-Subtracted Mission Average (ZSMA)' maps; the results generated by the Faint Source Model are contained in the 'Faint Source Model (FSM)' maps.

Appendix: Far-Infrared Emissivity of the Diffuse Ionized Medium

In Section 5.2.2, tracers of ionized gas toward the Lockman hole region were used to estimate the possible error in the zero level of the 100 μ m ISM template, as determined from intercepts of $\nu I_{ZG_S}(100~\mu\text{m}) - N(\text{H I})$ correlations, that result from our neglect of emission from H II associated dust. The 100 μ m emissivity per H nucleus was assumed to be the same in the ionized gas and the neutral atomic gas. Here, an attempt is made to determine the mean emissivity per H nucleus for the ionized gas at high galactic latitudes.

Previous efforts to measure far-infrared emission from the diffuse ionized medium have been inconclusive. Boulanger et al. (1995) found that the extended, low density H II region around the high latitude early B star α Vir has associated far-IR emission at a brightness that is consistent with a normal dust abundance, but this region may not be representative of the high latitude H II in general. Boulanger et al. (1996) searched for far-IR emission from the ionized medium by looking for a csc(|b|) dependence in residuals of their high latitude far-IR-N(H I) fits, which used DIRBE and FIRAS data from 100 to 1100 μ m. From the slopes of their $\csc(|b|)$ fits, they placed an upper limit on the far-IR brightness of a component of the H II gas that is not spatially correlated with N(H I). They found this limit to be consistent with a normal dust abundance in the ionized medium if about half of the far-IR emission from the ionized medium is uncorrelated with N(H I). Determination of the emissivity per H nucleus in the H II gas by this approach would require knowledge of the latitude dependence of H₂ associated emission, the latitude dependence of emissivity per H nucleus in the H I gas, and the degree of correlation of N(H II) with N(H I), which may also vary with latitude. Also using the FIRAS data, Fixsen et al. (1998) modeled the high latitude ISM emission with a combination of 158 μ m [C II] line emission, a tracer of ionized gas, and linear and quadratic terms in N(H I), a tracer of the neutral gas. Their analysis found that most of the high latitude far-IR emission correlated with the quadratic

term of the H I column density, and essentially no continuum emission correlated with the [C II] line emission. There have been a number of studies of correlations between far-IR and H α emission or between far-IR and microwave (largely free-free) emission at high latitudes (e.g., Kogut et al. 1996a, 1996b; De Oliveira-Costa et al. 1997; McCullough 1997; Kogut 1997). Interpretation of these correlations is not straightforward because they do not separately account for the far-IR emission from the dominant H I phase of the interstellar gas. Sodroski et al. (1997) derived mean far-IR emissivities for the extended low density ionized gas at low galactic latitudes by decomposing DIRBE maps into components that correlate with H I, CO, and radio continuum emission. This gas is probably associated with star forming regions, and is probably much denser and subject to a stronger radiation field than the diffuse warm ionized medium observed at high latitudes (e.g., Heiles, Reach, and Koo 1996; Lockman, Pisano, and Howard 1996).

Here, we use observations of H α intensity at high latitudes and observations of dispersion measure of pulsars at high |z| as tracers of the ionized gas. We compare results of regression fits of the forms $\nu I_{ZG_S}(100~\mu\text{m}) = A~N(\text{H~I}) + B~\text{and}~\nu I_{ZG_S}(100~\mu\text{m}) = C~N(\text{H~I}) + D~f(\text{H~II}) + E~\text{for data along high latitude lines of sight, where }I_{ZG_S}(100~\mu\text{m})~\text{is}$ DIRBE intensity after subtraction of IPD emission and f(H~II) is either extinction-corrected H α intensity or pulsar dispersion measure. The derived value of the parameter D can provide an estimate of the 100 μ m emissivity per H nucleus of the ionized medium, and the difference between parameters B and E provides an estimate of error in the zero level of 100 μ m ISM emission that is inferred if the ionized component is not accounted for.

Each tracer of ionized gas has advantages and disadvantages. Pulsar dispersion measure is a measure of ionized gas column density, but it pertains to a single line of sight rather than the solid angle sampled by the DIRBE beam, and it can significantly underestimate the total ionized column density along the line of sight if the pulsar is not above most of the ionized gas layer. The H α data used here were measured with a beam comparable to the DIRBE beam, and sample the entire path through the galaxy. However, H α emissivity is proportional to the square of the ionized gas density while 100 μ m emissivity is proportional to dust density. Another disadvantage of using H α is that it can be affected by extinction. An extinction correction has been applied to the H α intensities used here assuming the ratio of extinction coefficient to H α emissivity is constant along each line of sight (uniformly mixed extinction and emission), and the optical depth at H α is 0.04 N(H I) where N(H I) is in 10^{20} cm⁻². With these assumptions, the extinction correction factors range from 1.02 to 1.24 for the lines of sight used here.

The regression fitting has been done independently for five different regions or samples of positions. Sample 1 consists of 95 positions in a $10^{\circ} \times 12^{\circ}$ region centered at $l = 144^{\circ}$,

 $b=-21^{\circ}$, which was mapped in H α with a 0°.8 beam by Reynolds (1980). The region contains a number of elongated H α enhancements above a smooth background, and positions toward the brightest feature were excluded from our analysis because its estimated electron density is about 5 times higher than that of the other features (Reynolds et al. 1995). Sample 2 is a sample of 27 positions within 20 degrees of α Vir (at $l=317^{\circ}$, $b=50^{\circ}$) that were observed in H α by Reynolds (1985). Two positions within 1 degree of α Vir were not included in this sample because an enhanced 60 μ m to 100 μ m intensity ratio is observed at these positions. Sample 3 is a sample of 22 pulsar lines of sight at $|b| > 30^{\circ}$ that were observed in H α by Reynolds (1984, 1991b).

Samples 4 and 5 are different samples of pulsar lines of sight at $|b| > 20^{\circ}$, for which pulsar dispersion measure is used instead of $H\alpha$ as the tracer of ionized gas. Two different criteria were used to select pulsars likely to be at high |z| distances, so the dispersion measure traces most of the ionized gas layer. The first criterion is based on estimates of the z component of the characteristic pathlength L_c occupied by ionized gas between the Sun and the pulsar, $L_c \equiv (\int_0^d n_e ds)^2 / \int_0^d n_e^2 ds$, where d is the distance of the pulsar. Following an approach similar to that of Reynolds (1977, 1991b), lower limits to L_c were calculated for lines of sight to pulsars observed in H α by Reynolds (1984, 1991b), using $L_c > DM^2/EM$. Here DM is the pulsar dispersion measure and EM is the emission measure along the entire line of sight through the galactic disk, determined from the extinction-corrected $H\alpha$ intensity assuming an electron temperature of 8000 K. The calculated lower limit on $L_c | \sin b |$ ranges from 200 to 390 pc for lines of sight toward pulsars in four globular clusters at |z| > 4 kpc, and it is assumed that other pulsars with $L_c |\sin b| \ge 200$ pc are also above most of the ionized gas. Sample 4 consists of the 9 pulsar lines of sight selected by this criterion. Data for this sample are listed in Table 7. Sample 5 consists of 22 pulsar lines of sight at $|b| > 20^{\circ}$ for which $DM |\sin b|$ is greater than 0.6×10^{20} cm⁻², the minimum value of $DM \mid \sin b \mid$ for the globular cluster pulsars in Table 7. Some of the pulsars selected by this criterion may not be above most of the ionized gas layer if density enhancements in the ionized medium are common at high latitudes. The enhancements observed by Reynolds et al. (1995) in the $10^{\circ} \times 12^{\circ}$ region at $l = 144^{\circ}$, $b = -21^{\circ}$ have estimated N(H II) values ranging from 0.2 to 0.6×10^{20} cm⁻².

Results of the regression fits for Samples 1–3 are shown in Table 8 and results for Samples 4 and 5 are shown in Table 9. The errors listed were determined from the size of the 68% joint confidence region in parameter space. The fits for Samples 1 and 2 used H I column densities from the Leiden/Dwingeloo survey (Hartmann and Burton 1997), smoothed to the resolution of the DIRBE data, and the fits for the other samples used H I column densities from the Bell Laboratories survey (Stark et al. 1992). Except for the region around α Vir, the derived coefficient of the ionized gas tracer is consistent with zero

for each sample. (For comparison, the mean 100 μ m emissivities derived by Sodroski et al. (1997) for the extended low density ionized gas at low galactic latitudes correspond to $D_1 = 2.6 \pm 0.1 \text{ nW m}^{-2} \text{ sr}^{-1}/\text{Rayleigh}$ inside the solar circle and $1.8 \pm 0.2 \text{ nW m}^{-2} \text{ sr}^{-1}/\text{Rayleigh}$ outside the solar circle, assuming an ionized gas temperature of 8000 K.) The derived values of the isotropic terms B and E agree with each other within the uncertainties, and they are also consistent with the value of 19.8 nW m⁻² sr⁻¹ used for making the 100 μ m ISM template (Section 5.3).

Figure 19 illustrates correlations among the variables used for the regression fit for Samples 1, 2, and 4. Figure 19a shows linear fits to $\nu I_{ZG_S}(100~\mu\text{m})-N(\text{H I})$ correlations, Figure 19b shows linear fits to $H\alpha-N(\text{H I})$ or N(H II)-N(H I) correlations, and Figure 19c shows the correlation between residuals of the fit in Figure 19a and residuals of the fit in Figure 19b. Significant trends are not seen in Figure 19c, except for the region around α Vir.

The results of the regression fits and of Figure 19 show that 100 μ m emission has been detected from the ionized region around α Vir, but has not been detected from the general ionized medium at high latitudes. For Sample 1, the three sigma upper limit of $D_1 < 4.2$ nW m⁻² sr⁻¹/Rayleigh corresponds to an upper limit on the 100 μ m emissivity per H nucleus in the ionized medium of $D_2 < 12$ nW m⁻² sr⁻¹/ 10^{20} cm⁻², assuming electron density $n_e \le 0.2$ cm⁻³ and electron temperature of 8000 K (Reynolds et al. 1995). The results for Sample 3 give $D_2 < 4$ nW m⁻² sr⁻¹/ 10^{20} cm⁻² under the same assumptions. Comparison with the values of C found for these samples suggests that the 100 μ m emissivity per H nucleus is smaller in the ionized medium than in the neutral atomic medium. The results of the fits for Samples 4 and 5 are consistent with this conclusion, but the errors in the derived values of D_2 are large.

Differences in the electron density distribution along different lines of sight may cause errors in the results of the regression fits that use H α intensity as the ionized gas tracer. For the region of Sample 1, a crude model of the electron density distribution has been constructed. For each of the elongated features of enhanced H α emission, we use values derived by Reynolds et al. (1995) for the mean electron density and the mean linear size along the line of sight. The densities range from 0.08 to 0.23 cm⁻³. For the gas emitting the smooth H α background, we assume an electron density of 0.08 cm⁻³ (Reynolds 1991b) and determine its extent along each line of sight from the observed H α intensity, allowing for the contribution of each enhancement and assuming a gas temperature of 8000 K. The regression fit for Sample 1 was then repeated using ionized column density from the model instead of H α intensity. Results are $C = 16.0 \pm 1.1$ nW m⁻² sr⁻¹/10²⁰ cm⁻², $D_2 = 0.6 \pm 1.9$ nW m⁻² sr⁻¹/10²⁰ cm⁻², and $E = 26.1 \pm 8.3$ nW m⁻² sr⁻¹. The electron density model is

not unique, but the results are consistent with the conclusions that the 100 μ m emissivity per H nucleus is smaller in the ionized medium than in the neutral atomic medium, and that 100 μ m emission from the ionized medium does not cause significant error in the zero level of 100 μ m ISM emission inferred from the $\nu I_{ZG_S}(100 \ \mu\text{m}) - N(\text{H I})$ correlation.

Errors in the fit parameters can also occur if there is significant 100 μ m emission from H₂-associated dust along one or more lines of sight in a sample, but for the samples used here it appears that such errors are small. The regression fits were repeated excluding positions in each sample where the 100 μ m emission exceeds the H I correlated component of 100 μ m emission by more than about 20 nW m⁻² sr⁻¹. Reach et al. (1994, 1997) have presented evidence that such excess far-IR emission generally traces molecular gas. A small fraction of the positions was excluded for each sample, and the results were not significantly different from those of Table 8 and Table 9.

Other possible sources of error include errors in subtraction of IPD emission, and possible differences in the mean 100 μ m emissivity per H nucleus, within either the H I or H II gas, for different lines of sight. Such differences could be caused by differences in mean dust temperature or mean dust-to-gas mass ratio. Use of a small patch of the sky with a large number of lines of sight may reduce these sources of error, so the results for Sample 1 are considered to be the most reliable.

To summarize, a multiple regression analysis has been used to estimate an upper limit on the 100 μ m emissivity per H nucleus in the diffuse ionized gas at high latitudes. An upper limit of 12 nW m⁻² sr⁻¹/10²⁰ cm⁻² is obtained for a 10° × 12° region at $l=144^\circ$, $b=-21^\circ$. This value is 3/4 of the emissivity per H nucleus in the neutral atomic gas in the same region. Results for other samples of high latitude positions are consistent with this result, except a greater 100 μ m emissivity is found for ionized gas in the vicinity of the early B star α Vir. If our derived upper limit on the H II/H I emissivity ratio is valid for the general high latitude sky, the mean column density ratio N(H II)/N(H I) of about 1/3 (Reynolds 1991a) implies that on average less than ~20% of the total 100 μ m emission observed at high latitudes comes from the ionized gas phase. A low far-IR emissivity per H nucleus might be expected for the diffuse ionized medium since dust destruction by shocks is thought to be more efficient in the warm diffuse interstellar gas than in dense clouds (e.g., Seab 1987; McKee 1989; Jones et al. 1994, 1996). Future results from the Wisconsin H-Alpha Mapper survey (Tufte et al. 1996) will be useful for extending the type of analysis presented here to large areas of the high latitude sky.

REFERENCES

- Arendt, R. G., et al. 1994, ApJ, 425, L85
- Bernard, J. P., Boulanger, F., Desert, F. X., Giard, M., Helou, G., & Puget, J. L. 1994, A&A, 291, L5
- Binney, J., Gerhard, O., & Spergel, D. 1997, MNRAS, 288, 365
- Bissantz, N., Englmaier, P., Binney, J., & Gerhard, O. 1997, MNRAS, 289, 651
- Blitz, L. & Spergel, D. N. 1991, ApJ, 379, 631
- Boggess, N., et al. 1992, ApJ, 397, 420
- Boulanger, F., Abergel, A., Bernard, J.-P., Desert, F.-X., Lagache, G., Puget, J.-L., Burton,
 W. B., & Hartmann, D. 1995, in Unveiling the Cosmic Infrared Background, ed. E.
 Dwek, (Woodbury, NY: AIP), p. 87
- Boulanger, F., Abergel, A., Bernard, J.-P., Burton, W. B., Desert, F.-X., Hartmann, D., Lagache, G., & Puget, J.-L. 1996, A&A, 312, 256
- Burstein, D., & Heiles, C. 1982, AJ, 87, 1165
- Calbet, X., Mahoney, T., Hammersley, P. L., Garzon, F., & Lopez-Corredoira, M. 1996, ApJ, 457, L27
- Camilo, F., & Nice, D. J. 1995, ApJ, 445, 756
- COBE Diffuse Infrared Background Experiment (DIRBE) Explanatory Supplement, 1997, ed. M. G. Hauser, T. Kelsall, D. Leisawitz, and J. Weiland, COBE Ref. Pub. 97-A, (Greenbelt, MD: NASA/GSFC), available in electronic form from the NSSDC at http://www.gsfc.nasa.gov/astro/cobe/cobe_home.html
- Cohen, M. 1993a, AJ, 105, 1860
- Cohen, M. 1993b, private communication
- Cohen, M. 1994a, AJ, 107, 582
- Cohen, M. 1994b, private communication
- Cohen, M. 1995, ApJ, 444, 874
- Dall'Oglio, G., de Bernardis, P., Masi, F., Melchiorri, F., Moreno, G., & Trabalza, R. 1985, ApJ, 289, 609
- Davies, J. I., Trewhella, M., Jones, H., Lisk, C., Madden, A., & Moss, J. 1997, MNRAS, 288, 679
- de Geus, E., Bronfman, L., & Thaddeus, P. 1990, A&A, 268, 265

De Oliveira-Costa, A., Kogut, A., Devlin, D., Netterfield, C. B., Page, L. A., & Wollack, E. J. 1997, ApJ, 482, L17

de Vaucouleurs, G. 1995, in The Opacity of Spiral Disks, eds. J. L. Davies & D. Burstein, (Kluwer), 143

Dwek, E., et al. 1995, ApJ, 445, 716

Dwek, E., et al. 1997, ApJ, 475, 565

Dwek, E., et al. 1998, ApJ, submitted (Paper IV)

Elvis, M., Lockman, F. J., & Fassnacht, C. 1994, ApJS, 95, 413

Fixsen, D. J., Hinshaw, G., Bennett, C. L., & Mather. J. C. 1997, ApJ, 486, 623

Fixsen, D. J., Dwek, E., Mather, J. C., & Bennett, C. L. 1998, ApJ, submitted

Freudenreich, H. T., et al. 1994, ApJ, 429, L69

Freudenreich, H. T. 1996, ApJ, 468, 663

Fux, R. 1997, A&A, 327, 983

Gir, B.-Y., Blitz, L., & Magnani, L. 1994, ApJ, 434, 162

Halpern, J. P. 1996, ApJ, 459, L9

Haralick, R. M., Sternberg, S. R., & Zhuang, X. 1987, "Image Analysis Using Mathematical Morphology," IEEE Transactions on Pattern Analysis and Machine Intelligence, 9, 532

Hartmann, D., & Burton, W. B. 1997, Atlas of Galactic Neutral Hydrogen, (Cambridge:Cambridge University Press)

Hartmann, D., Magnani, L. & Thaddeus, P. 1998, ApJ, 492, 205

Hauser, M. G., et al. 1998, ApJ, submitted (Paper I)

Heiles, C., Reach, W. T., & Koo, B.-C. 1988, ApJ, 332, 313

Heiles, C., Reach, W. T., & Koo, B.-C. 1996, ApJ, 466, 191

Heithausen, A., Stacy, J. G., de Vries, H. W., Mebold, U., & Thaddeus, P. 1993, A&A, 268, 265

Holmberg, E. B. 1974, A&A, 35, 121

Johnson, H. L. 1966, ARA&A, 4, 193

Jones, A. P., Tielens, A. G. G. M., Hollenbach, D. J., & McKee, C. F. 1994, ApJ, 433, 797

Jones, A. P., Tielens, A. G. G. M., & Hollenbach, D. J. 1996, ApJ, 469, 740

Knude, J. 1996, A&A, 306, 108

Kelsall, T., et al. 1998, ApJ, submitted (Paper II)

Kogut, A., Banday, A. J., Bennett, C. L., Gorski, K. M., Hinshaw, G., & Reach, W. T. 1996a, ApJ, 460, 1

Kogut, A., Banday, A. J., Bennett, C. L., Gorski, K. M., Hinshaw, G., Smoot, G. F., & Wright, E. L. 1996b, ApJ, 464, L5

Kogut, A. 1997, AJ, 114, 1127

Lagache, G., Abergel, A., Boulanger, F., & Puget, J.-L. 1998, A&A, 333, 709

Lockman, F. J., Jahoda, K., & McCammon, D. 1986, ApJ, 302, 432

Lockman, F. J., Pisano, D. J., & Howard, G. J. 1996, ApJ, 472, 173

Lorimer, D. R., Lyne, A. G., Festin, L., & Nicastro, L. 1995, Nature, 376, 393

Magnani, L., & Onello, J. S. 1995, ApJ, 443, 169

McCullough, P. R. 1997, AJ, 113, 2186

McKee, C. F. 1989, in Interstellar Dust, ed. L. J. Allamandola & A. G. G. M. Tielens (Dordrecht: Kluwer), 431

Nordgren, T. E., Cordes, J. M., & Terzian, Y. 1992, AJ, 104, 1465

Odenwald, S., Newmark, J., & Smoot, G. 1998, ApJ, in press

Porcel, C., Battaner, E., & Jiménez-Vicente, J. 1997, A&A, 322, 103

Press, W. H., Teukolsky, S. A., Vetterling, W. T., & Flannery, B. P. 1992, Numerical Recipes in FORTRAN, Second Edition, (Cambridge: Cambridge University Press), 660

Reach, W. T., Koo, B.-C., & Heiles, C. 1994, ApJ, 429, 672

Reach, W. T., Wall, W. F., Hauser, M. G., Sodroski, T. J., Odegard, N., & Weiland, J. L. 1994, BAAS, 26, 1410

Reach, W. T., Wall, W. F., Odegard, N. 1998, ApJ, submitted

Reynolds, R. J. 1977, ApJ, 216, 433

Reynolds, R. J. 1980, ApJ, 236, 153

Reynolds, R. J. 1984, ApJ, 282, 191

Reynolds, R. J. 1985, AJ90, 92

Reynolds, R. J. 1991a, in IAU Symp. 144, The Interstellar Disk-Halo Connection in Galaxies, ed. H. Bloemen (Dordrecht: Kluwer), 337

Reynolds, R. J. 1991b, ApJ, 372, L17

- Reynolds, R. J. 1992, ApJ, 392, L35
- Reynolds, R. J., Tufte, S. L., Kung, D. T., McCullough, P. R., & Heiles, C. 1995, ApJ, 448, 715
- Rieke, G. H. & Lebofsky, M. J. 1985, ApJ, 288, 618
- Savage, B. D., Bohlin, R. C., Drake, J. F., & Budich, W. 1977, ApJ, 216, 291
- Seab, C. G. 1987, in Interstellar Processes, ed. D. J. Hollenbach & H. A. Thronson, Jr. (Dordrecht: Reidel), 491
- Silverberg, R. F., Hauser, M. G., Boggess, N. W., Kelsall, T. J., Moseley, S. H., & Murdock, T. L. 1993, in Infrared Spaceborne Remote Sensing, ed. M. S. Scholl (Proc. SPIE Conf. 2019), 180
- Sivan, J. P. 1974, A&AS, 16, 163
- Skrutskie, M. 1996, private communication
- Snowden, S. L., Hasinger, G., Jahoda, K., Lockman, F. J., McCammon, D., & Sanders, W. T. 1994, ApJ, 430, 601
- Sodroski, T. J., Dwek, E., Hauser, M. G., & Kerr, F. J. 1987, ApJ, 322, 101
- Sodroski, T. J., Dwek, E., Hauser, M. G., & Kerr, F. J. 1989, ApJ, 336, 762
- Sodroski, T. J., et al. 1994, ApJ, 428, 638
- Sodroski, T. J., et al. 1995, ApJ, 452, 262
- Sodroski, T. J., Odegard, N., Arendt, R. G., Dwek, E., Weiland, J. L., Hauser, M. G., & Kelsall, T. 1997, ApJ, 480, 173
- Stacy, J. G., Bertsch, D. L., Dame, T. M., Fichtel, C. E., Sreekumar, P., & Thaddeus, P. 1991, Proc. 22nd International Cosmic Ray Conference, Dublin, 141
- Stark, A. A., Gammie, C. F., Wilson, R. W., Bally, J., Linke, R. A., Heiles, C., & Hurwitz, M. 1992, ApJS, 79, 77
- Taylor, J. H., & Cordes, J. M., 1993, ApJ, 411, 674
- Taylor, J. H., Manchester, R. N., & Lyne, A. G. 1993, ApJS, 88, 529
- Tufte, S. L., Reynolds, R. J., Haffner, L. M., & Jaehnig, K. P. 1996, BAAS, 28, 890
- Wainscoat, R. J., Cohen, M., Volk, K., Walker, H. J., & Schwartz, D. E. 1992, ApJS, 83, 111
- Weiland, J. L., et al. 1994, ApJ, 425, L81
- Wheelock, S. L., et al. 1994, IRAS Sky Survey Atlas Explanatory Supplement, JPL Publication 94-11 (Pasadena: JPL)

Young, P. J. 1976, AJ, 81, 807

This preprint was prepared with the AAS LATEX macros v4.0.

- Fig. 1.— Full sky DIRBE intensity maps in Galactic Mollweide projection. Only IPD scattered light and emission have been removed. Intensities are scaled linearly in the ranges (-0.05,0.3), (-0.05,0.3), (-0.01,0.2), (0,0.2), (0,0.2), (0.5,3), (0,3), (0,15), (0,20), (0,20) MJy/sr at wavelengths from 1.25 to 240 μ m. Any intensities above or below these ranges appear white or black, respectively.
- Fig. 2.— The 2.2 μ m intensity map after application of bright source blanking. Intensity range is the same as in Figure 1.
- Fig. 3.— The 2.2 μ m intensity map of the Faint Source Model. Intensity range is the same as in Figure 1.
- Fig. 4.— $1.25 4.9 \mu m$ intensity maps after removal of emission from the IPD, and bright and faint Galactic stellar sources. Intensity ranges are the same as in Figure 1.
- Fig. 5.— Galactic intensity gradients. The left column shows the intensity after the IPD emission and bright sources have been removed as a function of $\csc(|b|)$. The right column shows the same data after the Faint Source Model has also been subtracted. $[\csc(15^{\circ}) \approx 4, \csc(30^{\circ}) = 2.0, \text{ and } \csc(60^{\circ}) = 1.15].$
- Fig. 6.— Ecliptic intensity gradients. Same as Fig. 5, but plotted with respect to ecliptic rather than Galactic latitude.
- Fig. 7.— Correlation of DIRBE 100 μ m intensities after subtraction of IPD emission with H I column density for (a) the North Ecliptic Pole region, (b) a region of low H I column density in Ursa Major, and (c) the region of high-latitude sky ($|b| > 25^{\circ}$, $|\beta| > 25^{\circ}$) covered by the Bell Laboratories H I survey. The solid lines show fits to the data as described in §5.2.1. Data above the short diagonal lines were excluded from the fitting.
- Fig. 8.— Correlations of Figure 7 averaged within bins along the fit lines. The bin boundaries used are perpendicular to the fit lines on plots where each variable is divided by its mean measurement error. The error bars are parallel to the bin boundaries and show the standard error of the mean for the data within each bin.
- Fig. 9.— (a) Ecliptic latitude dependence of DIRBE 100 μ m data after subtraction of IPD emission. Data at $\delta > -40^{\circ}$ are averaged within 10 degree bins in ecliptic latitude and the following bins in H I column density: $N({\rm H~I})/10^{20}~{\rm cm}^{-2}$ from 1.3 to 1.5 (diamonds), 1.5 to 1.7 (crosses), 1.7 to 1.9 (triangles), and 1.9 to 2.1 (squares). (b) The data averaged within 10 degree bins in Galactic latitude and the same bins in H I column density. (c) The data averaged within 20 degree bins in Galactic longitude and the same bins in H I column density.

- Fig. 10.— The ratio of H α intensity to dispersion measure as a function of H I column density, for lines of sight toward pulsars at $|b| > 20^{\circ}$ for which the z component of the characteristic pathlength occupied by ionized gas, $L_c|\sin b|$, is 200 pc or greater (see Appendix). These pulsars are probably above most of the ionized gas layer, and each dispersion measure is probably close to the total $N({\rm H~II})$ along the line of sight. Squares show data toward pulsars that are in globular clusters at |z| > 4 kpc.
- Fig. 11.— ISM correlation plots. These plots show the correlations that were used to derive the $R(\lambda)$ ISM colors at 12, 25, 60, 140, and 240 μ m. The lines indicate the weighted least-squares fit to the data.
- Fig. 12.— $3.5-240~\mu m$ intensity maps after removal of all IPD and Galactic foreground emission. Intensity ranges are the same as in Figure 1.
- Fig. 13.— Galactic intensity gradients. The left column shows the intensity after the IPD model, bright sources, and the Faint Source Model have been removed as a function of $\csc(|b|)$. The right column shows the same data after the ISM emission has also been subtracted.
- Fig. 14.— Ecliptic intensity gradients. Same as Fig. 13, but plotted with respect to ecliptic rather than Galactic latitude.
- Fig. 15.— The 240 μ m intensity map after removal of all foregrounds using the two-component ISM model (ISM2). Intensity range is the same as in Figure 1.
- Fig. 16.— Far-IR color-color plot. Each point represents the colors of a pixel where the 100 μ m brightness is > 40 MJy/sr. The straight line is the trend implied by the coefficients of the two-component ISM model (Equation 8). The crosses connected by lines indicate the expected colors for sources with emissivities $\sim \nu^2$ and temperatures from 16 to 22 K.
- Fig. 17.— The map of the reddening-free parameter, Q(1.25, 2.2, 3.5). Mid-latitude structures near $(l, b) = (90^{\circ}, +20^{\circ})$ and $(270^{\circ}, -20^{\circ})$ can be seen to correlate with ISM emission (e.g. the 240 μ m emission in Figure 1). Residual IPD errors cause artifacts (extended blue regions) at low ecliptic latitudes.
- Fig. 18.— Near-IR ISM correlation plots. These plots show the correlations that were used to derive the $R(\lambda)$ ISM colors at 3.5 and 4.9 μ m. The lines indicate least-squares fits to the data.
- Fig. 19.— Correlation plots of data for the lines of sight in Samples 1, 2, and 4. The error bars show 1σ measurement errors. The line shown in each panel is an unweighted least squares fit that minimizes the residuals in the ordinate. (a) Correlation of 100 μ m data

with H I column density. (b) Correlation of extinction-corrected H α intensity (for Samples 1 and 2) or H II column density (for Sample 4) with H I column density. (c) Correlation of residuals from the fit of (a) with residuals from the fit of (b).

Table 1. Effects of Faint Source Subtraction on Galactic Intensity Gradients

Wavelength (μm)	Before/After Faint Source Subtraction	Gradient ^a (nW m ⁻² sr ⁻¹ / csc(b))	Correlation Coefficient ^a	
1.25	before	192.7 ± 0.7	0.61	
1.25	after	-21.6 ± 0.7	-0.09	
2.2	before	74.3 ± 0.3	0.56	
2.2	after	-16.8 ± 0.3	-0.15	
3.5	before	29.4 ± 0.1	0.45	
3.5	after	-4.6 ± 0.1	-0.07	
4.9	before	11.4 ± 0.1	0.24	
4.9	after	-0.4 ± 0.1	-0.005	

 $^{^{\}mathrm{a}}|b| > 30^{\circ}$

Table 2. Parameters of 100 $\mu \mathrm{m}$ – H I Correlations

Region	Center of Region	$\nu I_0(100 \ \mu \text{m})$ (nW m ⁻² sr ⁻¹)	$(\text{nW m}^{-2} \text{ sr}^{-1} / 10^{20} \text{ cm}^{-2})$	$\chi^2_{ u}$	Correlation Coefficient
North Ecliptic Pole	(l, b) = (96, 30) $(\lambda, \beta) = (0, 90)$	17.3 ± 1.7	19.1 ± 0.5	3.3	0.95
Lockman Hole	(l,b) = (150, 53) $(\lambda, \beta) = (136, 45)$	22.3 ± 0.5	17.6 ± 0.5	4.4	0.75
b > 25, $ \beta > 25, \delta > -40$		21.2 ± 0.6	18.6 ± 0.3	12.9	0.81

Table 4. Parameters of IR Correlations

Wavelength (μm)	$R(\lambda)^{\mathrm{a}}$	Dispersion (nW m ⁻² sr ⁻¹)	Correlation Coefficient	Region
1.25				
2.2	• • •	• • •		
3.5	0.00183 ± 0.00001	17.6	0.79	b
4.9	0.00291 ± 0.00003	22.0	0.66	b
12	0.0462 ± 0.0001	15.2	0.94	$b > 10^{\circ}, \beta > 70^{\circ}$
25	0.0480 ± 0.0002	8.5	0.93	$b > 10^{\circ}, \beta > 70^{\circ}$
60	0.171 ± 0.0003	4.0	0.91	$ b > 30^{\circ}, \beta > 40^{\circ}$
100	1.00	• • •		•••
140	1.696 ± 0.008	57.2	0.52	$ b > 45^{\circ}$
240	1.297 ± 0.005	19.4	0.62	$ b > 45^{\circ}$

 $^{^{\}rm a} = I_{\nu}(\lambda)/I_{\nu}(100 \ \mu {\rm m})$

^bFor 3.5 and 4.9 μ m the regions used were $|b| < 30^{\circ}, |\beta| > 40^{\circ},$ and $54^{\circ} < l < 138^{\circ}$ and $234^{\circ} < l < 318^{\circ}.$

 ${\it Table 5.} \quad {\it Effects of ISM Subtraction on Galactic Intensity Gradients}$

Wavelength (μm)	Before/After ISM Subtraction	Gradient ^a $(nW m^{-2} sr^{-1} / csc(b))$	Correlation Coefficient ^a
3.5	before	-4.6 ± 0.1	-0.07
3.5	after	-9.2 ± 0.1	-0.15
4.9	before	-0.4 ± 0.1	-0.005
4.9	after	-5.7 ± 0.1	-0.13
12	before	-36.6 ± 0.5	-0.17
12	after	-70.6 ± 0.4	-0.37
25	before	-45.0 ± 0.3	-0.33
25	after	-62.0 ± 0.3	-0.45
60	before	24.5 ± 0.1	0.50
60	after	1.1 ± 0.1	0.03
100	before	76.1 ± 0.3	0.51
100	after	-3.3 ± 0.1	-0.04
140	before	128.7 ± 0.6	0.43
140	after	34.1 ± 0.5	0.16
240	before	55.6 ± 0.2	0.46
240	after	16.3 ± 0.2	0.22

 $^{^{\}rm a}|b|>30^{\rm \circ}$

Table 8. Results of Fits Using $N({\rm H~I})$ and $I({\rm H}\alpha)$

Sample	$\frac{A}{(\frac{\text{nW m}^{-2} \text{ sr}^{-1}}{10^{20} \text{ cm}^{-2}})}$	$B \text{ (nW m}^{-2} \text{ sr}^{-1}\text{)}$	$\frac{C}{(\frac{\text{nW m}^{-2} \text{ sr}^{-1}}{10^{20} \text{ cm}^{-2}})}$	$\frac{D_1}{\left(\frac{\text{nW m}^{-2} \text{ sr}^{-1}}{\text{Rayleigh}}\right)}$	$E \text{ (nW m}^{-2} \text{ sr}^{-1}\text{)}$	$N_{ m points}$
1	16.2 ± 1.1	26.9 ± 6.3	16.3 ± 1.1	-0.3 ± 1.5	27.4 ± 8.3	95
2	21.9 ± 2.4	42 ± 12	19.5 ± 1.6	10.1 ± 2.3	25.2 ± 9.5	27
3	23.0 ± 1.4	16.6 ± 4.3	23.1 ± 1.8	0.1 ± 0.4	16.5 ± 5.4	22

Note. — Fits of the forms $\nu I_{ZG_S}(100~\mu\mathrm{m}) = A~N(\mathrm{H~I}) + B$ and $\nu I_{ZG_S}(100~\mu\mathrm{m}) = C~N(\mathrm{H~I}) + D_1~I(\mathrm{H}\alpha)~\tau/(1-e^{\tau}) + E$.

Table 9. Results of Fits Using $N({\rm H~I})$ and Dispersion Measure

Sample	$\frac{A}{(\frac{\text{nW m}^{-2} \text{ sr}^{-1}}{10^{20} \text{ cm}^{-2}})}$	$B = (\text{nW m}^{-2} \text{ sr}^{-1})$	$\frac{C}{(\frac{\text{nW m}^{-2} \text{ sr}^{-1}}{10^{20} \text{ cm}^{-2}})}$	$\frac{D_2}{(\frac{\text{nW m}^{-2} \text{ sr}^{-1}}{10^{20} \text{ cm}^{-2}})}$	$E \text{ (nW m}^{-2} \text{ sr}^{-1}\text{)}$	$N_{ m points}$
4 5	24.3 ± 2.2 22.7 ± 3.1	12.3 ± 5.8 18.9 ± 12.5	21.2 ± 3.7 29.4 ± 5.0	15.6 ± 19.6 -41.3 ± 33.1	5.9 ± 9.0 42.9 ± 20.9	9 22

Note. — Fits of the forms $\nu I_{ZG_S}(100~\mu\mathrm{m}) = A~N(\mathrm{H~I}) + B$ and $\nu I_{ZG_S}(100~\mu\mathrm{m}) = C~N(\mathrm{H~I}) + D_2~DM + E$.

This figure "fig1a.jpg" is available in "jpg" format from:

This figure "fig1b.jpg" is available in "jpg" format from:

This figure "fig1c.jpg" is available in "jpg" format from:

This figure "fig2.jpg" is available in "jpg" format from:

This figure "fig3.jpg" is available in "jpg" format from:

This figure "fig4.jpg" is available in "jpg" format from:

This figure "fig5.gif" is available in "gif" format from:

This figure "fig6.gif" is available in "gif" format from:

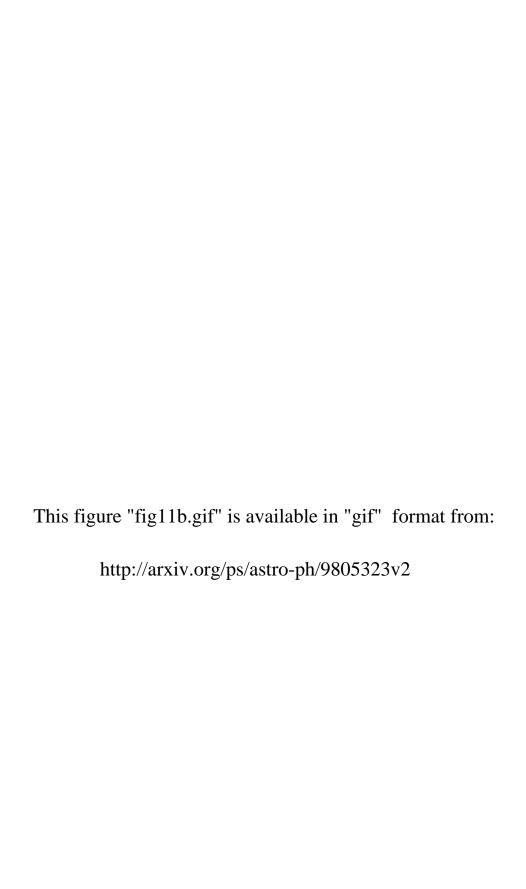
This figure "fig7.gif" is available in "gif" format from:

This figure "fig8.gif" is available in "gif" format from:

This figure "fig9.gif" is available in "gif" format from:

This figure "fig10.gif" is available in "gif" format from:

This figure "fig11a.gif" is available in "gif" format from: http://arxiv.org/ps/astro-ph/9805323v2



This figure "fig12a.jpg" is available in "jpg" format from:

This figure "fig12b.jpg" is available in "jpg" format from:

This figure "fig13a.gif" is available in "gif" format from:

This figure "fig13b.gif" is available in "gif" format from: http://arxiv.org/ps/astro-ph/9805323v2

This figure "fig13c.gif" is available in "gif" format from:

This figure "fig14a.gif" is available in "gif" format from:

This figure "fig14b.gif" is available in "gif" format from: http://arxiv.org/ps/astro-ph/9805323v2

This figure "fig14c.gif" is available in "gif" format from:

This figure "fig15.jpg" is available in "jpg" format from:

This figure "fig16.gif" is available in "gif" format from:

This figure "fig17.jpg" is available in "jpg" format from:

This figure "fig18.gif" is available in "gif" format from:

This figure "fig19.gif" is available in "gif" format from:

 $\label{eq:table 3}$ H II and H_2 in the Lockman Hole and NEP Regions

Observations	$ Position \\ (\mathit{l},\mathit{b}) $	Inferred Column Density $(10^{20}~{\rm cm}^{-2})$	H I Column Density $(10^{20}~{\rm cm^{-2}})$	Reference to Column 1 Data
${\rm DM} = 0.278 \times 10^{20}~{\rm cm}^{-2}~{\rm toward~PSR~J1012} + 5307$	$160.4,\ 50.9$	$N({ m H~II})\sim0.6$	0.69	Lorimer et al. 1995
$\rm I(H\alpha)<0.15\;R^a$	150.5, 53.0	$N({\rm H~II})<0.20^{\rm a}$	0.54	Jahoda et al. 1990
$I(H\alpha)=0.20{\pm}0.06~R$	160.0, 50.0	$N({ m H~II}) = 0.27 {\pm} 0.08$	0.74	Jahoda et al. 1990
RMS Noise of $^{12}\mathrm{CO}$ spectrum = 0.1 K	$10^{\circ} \times 10^{\circ}$ at 153, 53	$N({ m H}_2)< 1.2^{ m a}$	0.5 - 1.2	Stacy et al. 1991
RMS Noise of $^{12}\mathrm{CO}$ spectrum = 0.05 K	toward H I emission peaks in NEP Region	$N({ m H_2})<0.6^{ m a}$	< 8.1	Elvis et al. 1994

 $^{^{\}mathrm{a}}3\sigma$ limit

NOTE.—H α intensities converted to column densities assuming $I({\rm H}\alpha)/N({\rm H~II})=0.75~{\rm Rayleigh}/10^{20}~{\rm cm}^{-2}$

CO data converted to $N({\rm H_2})$ from linewidth of 1 km s⁻¹ and $N({\rm H_2})/W({\rm CO}) < 4 \times 10^{20}~{\rm mol~cm^{-2}~(K~km~s^{-1})^{-1}}$

TABLE 6
Systematic Uncertainties

Wavelength	Detector Offset	Detector Gain	Zodiacal Light Uncertainty	Bright Source Blanking	Faint Source Model	$I_0(100~\mu\mathrm{m})$ from H I	$R(\lambda)$ Uncertainty	Total Systematic
	Uncertainty	Uncertainty		${ m Uncertainty}$	Uncertainty	${ m Uncertainty}$		Uncertainty
$(\mu\mathrm{m})$	$(nW m^{-2} sr^{-1})$		$(nW m^{-2} sr^{-1})$	$({\rm nW~m^{-2}~sr^{-1}})$	$(nW m^{-2} sr^{-1})$	$({\rm nW~m^{-2}~sr^{-1}})$	$({\rm nW~m^{-2}~sr^{-1}})$	$(nW m^{-2} sr^{-1})$
1.25	0.05	0.031	15.	2.3	15	• • •		21
2.2	0.028	0.031	6.	0.6	10	• • •		12
3.5	0.015	0.031	2.	0.2	6	0.4	0.2	6
4.9	0.010	0.030	6.	0.02	5	0.5	0.3	8
12	0.015	0.051	138.	small	small	3.0	3.8	138
25	0.010	0.151	156.	small	small	1.5	1.2	156
60	1.34	0.104	27.			2.2	1.3	27
100	0.81	0.135	6.			5.0	5.3	9
140	5	0.106	2.3			9.5	4.8	12
240	2	0.116	0.5			4.2	2.3	5

TABLE 7

Pulsar Lines of Sight Used in Regression Fits

PSR	l	b	Cluster Membership	$\mathbf{z}^{\mathbf{a}}$ (kp c)	$L_{ c} sin(b) $ lower limit (pc)	n_c upper limit (cm ⁻³)	${ m DM^b}$ ${ m 10^{20}} cm^{-2}$	$N(H I)^{c}$ $10^{20} cm^{-2}$
B0148-06	160.4	-65.0			$400{\pm}210$	$0.056 \!\pm\! .029$	$0.77 \!\pm\! 0.09$	2.3
B0940+16	216.6	45.4	• • •		200± 80	$0.072 \!\pm\! .026$	$0.62\!\pm\!0.09$	3.2
B1310+18	333.0	79.8	in M53	17.8	390± 90	$0.060 \pm .013$	$0.74\!\pm\!0.05$	1.9
B1508+55	91.3	52.3			$260 {\pm} 160$	$0.059 \pm .035$	0.60 ± 0.00	1.4
B1516+02A,B	3.9	46.8	in M5	5.1	$290\pm\ 50$	$0.078 \pm .014$	$0.94 \!\pm\! 0.02$	3.8
B1541+09	17.8	45.8	•••		$280 {\pm} 110$	$0.089 \!\pm\! .034$	1.08 ± 0.00	3.3
B1639+36A,B	59.0	40.9	in M13	4.5	$370 \pm\ 70$	$0.054 \!\pm\! .010$	$0.94 \!\pm\! 0.00$	1.5
B2113+14	64.5	-23.4	•••		$290\pm~50$	$0.077 \pm .014$	1.74 ± 0.01	6.5
B2127+11A-H	65.0	-27.3	in M15	-4.6	$200\pm~50$	$0.152 \pm .038$	2.07 ± 0.00	6.5

^aCluster z distance from Harris (1996)

^bFrom Taylor, Manchester, and Lyne (1993)

^cFrom Bell Laboratories H I survey (Stark et al. 1992)